

AFIT/GM/ENP/98M-07

**PERFORMANCE OF IMAGING LASER RADAR
IN RAIN AND FOG**

THESIS

**Kathleen M. Campbell
2Lt, United States Air Force**

AFIT/GM/ENP/98M-07

19980410 077

Approved for public release; distribution unlimited

The views expressed in this thesis are those of the author and do not reflect the official policy or position of the United States Air Force, the Department of Defense, the U.S. Government, or any agency mentioned in the document.

AFIT/GM/ENP/98M-07

PERFORMANCE OF IMAGING LASER RADAR
IN RAIN AND FOG

THESIS

Presented to the Faculty of the School of Engineering
Air Education and Training Command
In Partial Fulfillment of the
Requirements for the Degree of
Master of Science (Meteorology)

Kathleen M. Campbell, B.S.
2Lt, United States Air Force

March 1998

Approved for public release; distribution unlimited

PERFORMANCE OF IMAGING LASER RADAR
IN RAIN AND FOG

Kathleen M. Campbell, B.S.
2Lt, USAF

Approved:

Clifton E. Dungey
Maj Clifton E. Dungey
Chairman, Advisory Committee

5 Mar 98
Date

Jeffrey W. Grantham
Maj Jeffrey W. Grantham
Member, Advisory Committee

5 Mar 98
Date

Craig Largent
Capt Craig Largent
Member, Advisory Committee

6 Mar 98
Date

Acknowledgments

Whenever a project of this magnitude is undertaken, anyone could begin to feel overwhelmed and a little stressed. And lucky for me, I was struck with the same feelings. Very soon after I chose this topic, I realized the challenge I faced and the importance of the issue. But I knew that there would be several important people who would help me to be successful in this new mission.

I would first like to thank my thesis advisor Maj. Clifton Dungey. His guidance, understanding, and knowledge were instrumental in the completion of this thesis. He helped me stay on track and focused on the important issues, plus he allowed me the important opportunity of learning along the way. I would also like to thank the members of my thesis committee, Capt. Craig Largent and Maj. Jeff Grantham, who is also my thesis sponsor. By bringing their special expertise to this thesis, I was able to provide useful and meaningful information for the sponsoring agency. Finally, I am eternally grateful to Lt. Eddie Meidunas. His patience and hard work were essential in all aspects of this thesis, and he was always a willing helper. No task was too big. No question too silly. ¡Muchas gracias señor!

I would be amiss if I failed to take a moment to thank the members of GM-98M, my AFIT classmates. I have always been amazed at how well we get along, and that has been one of the most important parts of my AFIT experience. We've grumbled, griped, laughed, and cheered together, and now we head out into the real world again to make our positive contributions to society. May our paths always cross.

And to the meteorology faculty of AFIT I also owe a special thank you. When I first came to AFIT, I was a little skeptical of what to expect from all of you. You have

continually impressed me with your knowledge, insight, and helpful spirits. A good portion of my AFIT experience is filled with positive memories of you, from both inside and out of the classroom.

And finally, I'd like to thank my husband Andrew and my parents. They have patiently listened when I thought I was going to lose the battle against stress and work, but they have always been willing to listen. Their love and support have been amazing. And I only wish I can begin to repay a fraction of that.

2Lt. Kathleen Mary Campbell

Table Of Contents

Acknowledgments.	iii
List of Figures.	viii
List of Tables.	xii
Abstract.	xiv
I. Introduction.	1
1.1 Background.	1
1.2 Specific Problem.	3
1.3 Research Objectives.	3
1.4 Limitations.	4
1.5 Overview.	5
II. Background.	6
2.1 Mie Scattering Theory.	6
2.2 Attenuation Due to Fog.	7
2.2.1 Chylek, 1978.	8
2.2.2 Pinnick, et al., 1978.	9
2.2.3 Pinnick, et al., 1979.	10
2.2.4 Tonna, 1991.	11
2.3 Attenuation by Rain.	13
2.3.1 Jelalian, 1992.	13

2.4 Mean Free Path	14
2.4.1 Sears and Salinger, 1975	14
III. Procedure	19
3.1 Image Analysis	19
3.2 Instrumentation	22
3.3 Meteorological Data	24
3.4 Data and Graphical Analysis	26
3.4.1 Data Analysis	26
3.4.2 Graphical Analysis	27
3.4.3 Control Charts	28
3.4.4 Mean Free Path and Survival Equation	29
IV. Results	32
4.1 Correlation Coefficients Between Several Variables	32
4.2 Graphical Analysis of Variables	34
4.2.1 Dropouts and Visibility vs. Time	34
4.2.2 Dropouts and Rainfall Rate vs. Time	38
4.2.3 False Returns and Visibility vs. Time	39
4.2.4 False Return and Rainfall Rate vs. Time	43
4.2.5 Dropouts vs. Visibility	44
4.2.6 Dropouts vs. Rainfall Rate	49
4.2.7 False Returns vs. Visibility	51
4.2.8 False Returns vs. Rainfall Rate	56

4.2.9 Extinction and Returns vs. Time.....	57
4.3 Control Charts for Various Variables.....	62
4.3.1 January 3, 1997.....	62
4.3.2 February 19, 1997.....	64
4.3.3 February 24, 1997.....	66
4.3.4 February 25, 1997.....	68
4.3.5 February 26, 1997.....	71
4.3.6 February 27, 1997.....	72
4.3.7 February 28, 1997.....	75
4.4 Mean Free Path and Survival Equation.....	76
4.4.1 Mean Free Path for Each Day.....	77
4.4.2 Survival Equation and Calculated Number of Returns.....	79
4.4.3 Minimum Diameter Calculations.....	80
4.4.4 Use of Theoretical Rainfall Rate Distribution.....	82
4.5 Solar Contamination in the Operation of the Ladar System.....	84
V. Summary, Conclusions, and Recommendations.....	93
5.1 Summary.....	93
5.2 Conclusions.....	93
5.3 Recommendations.....	94
References.....	95
Vita.....	96

List of Figures

Figure	Page
4.1 Number of dropouts and visibility with respect to time, January 3, 1997.	35
4.2 Number of dropouts and visibility with respect to time, February 19, 1997.	35
4.3 Number of dropouts and visibility with respect to time, February 24, 1997.	36
4.4 Number of dropouts and visibility with respect to time, February 25, 1997.	36
4.5 Number of dropouts and visibility with respect to time, February 26, 1997.	37
4.6 Number of dropouts and visibility with respect to time, February 27, 1997.	37
4.7 Number of dropouts and visibility with respect to time, February 28, 1997.	38
4.8 Number of dropouts and rainfall rate with respect to time, February 24, 1997.	38
4.9 Number of dropouts and rainfall rate with respect to time, February 25, 1997.	39
4.10 Number of false returns and visibility with respect to time, January 3, 1997.	40
4.11 Number of false returns and visibility with respect to time, February 19, 1997.	40
4.12 Number of false returns and visibility with respect to time, February 24, 1997.	41
4.13 Number of false returns and visibility with respect to time, February 25, 1997.	41
4.14 Number of false returns and visibility with respect to time, February 26, 1997.	42
4.15 Number of false returns and visibility with respect to time, February 27, 1997.	42
4.16 Number of false returns and visibility with respect to time, February 28, 1997.	43

4.17	Number of false returns and rainfall rate with respect to time, February 24, 1997.....	43
4.18	Number of false returns and rainfall rate with respect to time, February 25, 1997.....	44
4.19	Number of dropouts compared to visibility for January 3, 1997.....	45
4.20	Number of dropouts compared to visibility for February 19, 1997.....	45
4.21	Number of dropouts compared to visibility for February 24, 1997.....	46
4.22	Number of dropouts compared to visibility for February 25, 1997.....	46
4.23	Number of dropouts compared to visibility for February 26, 1997.....	47
4.24	Number of dropouts compared to visibility for February 27, 1997.....	47
4.25	Number of dropouts compared to visibility for February 28, 1997.....	48
4.26	Composite graph of number of dropouts versus visibility.....	49
4.27	Number of dropouts compared to rainfall rate for February 24, 1997.....	50
4.28	Number of dropouts compared to rainfall rate for February 25, 1997.....	50
4.29	Composite graph of number of dropouts versus rainfall rate.....	51
4.30	Number of false returns compared to visibility for January 3, 1997.....	52
4.31	Number of false returns compared to visibility for February 19, 1997.....	52
4.32	Number of false returns compared to visibility for February 24, 1997.....	53
4.33	Number of false returns compared to visibility for February 25, 1997.....	53
4.34	Number of false returns compared to visibility for February 26, 1997.....	54
4.35	Number of false returns compared to visibility for February 27, 1997.....	54
4.36	Number of false returns compared to visibility for February 28, 1997.....	55
4.37	Composite graph of number of false returns versus visibility.....	55
4.38	Number of false returns compared to rainfall rate on February 24, 1997.....	56

4.39	Number of false returns compared to rainfall rate on February 25, 1997.....	56
4.40	Composite graph of number of false returns versus rainfall rate	57
4.41	Extinction versus time with dropouts, January 3, 1997.....	58
4.42	Extinction versus time with dropouts, February 19, 1997.....	58
4.43	Extinction versus time with dropouts, February 24, 1997.....	59
4.44	Extinction versus time with dropouts, February 25, 1997.....	59
4.45	Extinction versus time with dropouts, February 26, 1997.....	60
4.46	Extinction versus time with dropouts, February 27, 1997.....	60
4.47	Extinction versus time with dropouts, February 28, 1997.....	61
4.48	Composite graph of number of dropouts versus extinction	62
4.49	Statistical control chart for number of dropouts over time, January 3, 1997..	63
4.50	Statistical control chart for number of false returns over time, January 3, 1997.....	63
4.51	Statistical control chart for visibility over time, January 3, 1997.....	64
4.52	Statistical control chart for number of dropouts over time, February 19, 1997.....	65
4.53	Statistical control chart for number of false returns over time, February 19, 1997.....	65
4.54	Statistical control chart for visibility over time, February 19, 1997.....	66
4.55	Statistical control chart for number of dropouts over time, February 24, 1997.....	66
4.56	Statistical control chart for number of false returns over time, February 24, 1997.....	67
4.57	Statistical control chart for rainfall rate over time, February 24, 1997.....	67
4.58	Statistical control chart for visibility over time, February 24, 1997.....	68

4.59	Statistical control chart for number of dropouts over time, February 25, 1997.....	69
4.60	Statistical control chart for number of false returns over time, February 25, 1997.....	69
4.61	Statistical control chart for rainfall rate over time, February 25, 1997.....	70
4.62	Statistical control chart for visibility over time, February 25, 1997.....	70
4.63	Statistical control chart for number of dropouts over time, February 26, 1997.....	71
4.64	Statistical control chart for number of false returns over time, February 26, 1997.....	72
4.65	Statistical control chart for visibility over time, February 26, 1997.....	72
4.66	Statistical control chart for number of dropouts over time, February 27, 1997.....	73
4.67	Statistical control chart for number of false returns over time, February 27, 1997.....	74
4.68	Statistical control chart for visibility over time, February 27, 1997.....	74
4.69	Statistical control chart for number of dropouts over time, February 28, 1997.....	75
4.70	Statistical control chart for number of false returns over time, February 28, 1997.....	76
4.71	Statistical control chart for visibility over time, February 28, 1997.....	76
4.72	Marshall-Palmer raindrop size distribution.....	78
4.73	Comparison of the radiance of the sun to the radiance of a black object at 200 km (at the horizon).....	87

List of Tables

Table	Page
3.1 Total number of pixels for the target panel on each of the seven days.	21
3.2 Total number of pixels used for the portion of open sky during the false return analysis.	21
3.3 Example spreadsheet file, used in organizing the data sets for each day.	25
4.1 Correlation coefficients for dropout percentage and visibility.	33
4.2 Correlation coefficients for dropout percentage and rainfall rate.	33
4.3 Correlation coefficients for false return percentage and visibility.	33
4.4 Correlation coefficients for false return percentage and rainfall rate.	33
4.5 Correlation coefficients for extinction and number of dropouts	33
4.6 Mean free path on February 24, 1997 and February 25, 1997 over time.	79
4.7 Number of returns computed using the survival equation for February 24, 1997 and February 25, 1997.	80
4.8 Mean free path computed with the 3.0-mm minimum diameter for February 24, 1997 and February 25, 1997.	81
4.9 Number of returns computed with the 3.0-mm minimum diameter for February 24, 1997 and February 25, 1997.	82
4.10 Theoretical rainfall rate distribution, mean free path, and calculated number of returns.	83
4.11 Drop distribution and number density for 1-mm/hr rainfall rate.	90
4.12 Drop distribution and number density for 5-mm/hr rainfall rate.	90
4.13 Drop distribution and number density for 10-mm/hr rainfall rate.	90
4.14 Total cross sectional area of the raindrops within the laser beam cone for all three rainfall rates.	91

4.15 Number of drops calculated to be within the laser beam, according to rainfall rate.	91
--------------------------------------------------------------------------------------------------	----

Abstract

The Air Force is currently developing imaging laser radar systems (ladar) for use on precision guided munitions and other imaging systems. Scientists at Eglin Air Force Base, in conjunction with Wright Laboratories, are testing a 1.06- μ m wavelength ladar system and need to understand the weather effects on the ladar images. As the laser beam propagates through the atmosphere, fog droplets and raindrops can cause image degradation, and these image degradations are manifested as either dropouts or false returns. An analysis of the dropouts and false returns helped to quantify the performance of the system in adverse weather conditions. Statistical analysis of the images showed non-linear relationships existed between variables, plus graphical analysis demonstrated the behavior of the dropouts and false returns with changing weather conditions. Statistical control charts identified the weather as a significant influence on the quality of the ladar images. By focusing on the false return data, a study of mean free path and the survival equation was accomplished. The mean free path was derived from the rainfall rate, and this mean free path was used in the survival equation to calculate an expected number of false returns for an image. This work led to the hypothesis that raindrops with a diameter of 3.0 mm and larger were causing the false returns seen in the images. However, further analysis revealed that a 3.0-mm raindrop was not capable of scattering enough energy to be detected by the system. It was then hypothesized that the system detector was also picking up solar spectrum energy scattered by raindrops, and that this detector was unable to distinguish between solar energy and laser energy scattered by raindrops.

I. Introduction

1.1 - Background

In his 1993 article “Will Ladar be the DoD’s Next Quantum Leap?”, John Keller describes how laser detection and ranging (LADAR) has come to the forefront of radar technology. This system’s capabilities include several not attainable via conventional radar, such as detection of stealth aircraft, submarines, underwater mines, poison gas and other biological agents, severe air turbulence, and windshear. Due to these new capabilities, ladar is proving to be superior in imaging applications, especially when used with precision guided munitions.

Ladar demonstrates three advantages over conventional radar systems—better resolution, stable signature, and 3-D image capability. The improved resolution comes from the fact that ladar uses shorter wavelengths than radar. Some versions of the system resolve wires, cables, and antennas at virtually any angle, which is helpful when piloting helicopters. Another advantage is the stability of the ladar signal. This results in a more reliable match with pre-stored imaging data, so targets are recognized more often with fewer false alarms. Finally, ladar produces a 3-D image of the target. This makes ladar particularly attractive for automatic target recognition systems. The on-board computer considers the target from several different angles before deciding whether it matches stored images for the target.

However, ladar falls short in two areas when compared to conventional millimeter radar. One, radar has a longer range than ladar. The longer wavelength allows the beam to propagate a longer distance. The beam can pass by more particles simply because they

are too small to affect the beam. And two, millimeter radar can operate in more severe environmental conditions, making it more all-weather. Millimeter radar outperforms ladar in smoke, fog, and other adverse weather conditions.

Ladar became important to the Air Force for improving the performance of precision guided munitions. Systems such as the small smart bomb, anti-materiel munitions, and air superiority missile programs could use the ranging, imaging, and discriminating capabilities to improve performance and accuracy. Ladar's ability to discriminate between targets located near one another and to guide the munition to the correct target makes this new technology particularly attractive.

Scientists at Elgin AFB, FL currently support the laser radar program for Wright Labs. A neodymium yttrium aluminum garnet (Nd:YAG) pulsed laser, 1.064- μ m wavelength, scans over a field of predetermined targets, and the performance of the laser under differing weather conditions (rain, fog, or other low visibility scenarios) is recorded. The generated image is analyzed to determine irregularities that appear in the image.

Irregularities come from false returns and dropouts. False returns happen when particles in the atmosphere scatter the laser beam energy back to the receiver. The returns appear as closer than expected returns on the image because the beam scatters before it reaches the predetermined target. Dropouts occur when the return signal is too weak to be detected. A weak return appears if the beam has been scattered in a direction other than back toward the detector or when there is no target to reflect the beam. Both of these errors degrade the performance of the ladar, limiting its imaging capabilities. By keeping track of the number of false returns and dropouts, scientists can statistically analyze what happens to the laser beam as it propagates through the atmosphere.

Threshold values for atmospheric conditions can then be determined to predict performance of the system. Hopefully, a model can be built to describe the behavior of the ladar under various atmospheric conditions. This would then allow users of the system to determine when it is best to use the system and what kind of performance to expect when the system operates.

1.2 - Specific Problem

Disruption of the laser radar image of a target occurs when one of two things happens. The first is called a dropout, when a pixel area shows no return. If the energy return falls below a certain threshold, the laser registers no return and assigns that pixel the maximum range. A dropout happens when the laser beam is attenuated or scattered by a particle in the atmosphere in a direction other than that of the ladar. So in an image of a specific target (a region of pixels with high power returns), a dropout pixel indicates the same power return as an area of open sky (a region of almost no power return, maximum range). The second type of image disruption is called a false return. False-return pixels appear as higher-than-expected power returns when compared to the target region of sky. When a particle in the atmosphere scatters the laser beam before it reaches the target, this return pixel is registered as a false return. A region of open sky is used to identify false returns, since only maximum range returns are expected.

1.3 - Research Objectives

In previous laser research, a single laser beam propagated through an atmosphere with known weather conditions, and the behavior of this single beam was recorded and

analyzed. The laser radar used in this thesis is a scanning laser, so the study of this system required thinking about numerous laser beams propagating through the atmosphere. This thesis involved looking at the dropouts and false returns on a radar image caused by particles in the atmosphere. To predict future performance of the system, an understanding of the degradation of the image by the weather will prove important. The data collected from the laser images by Labview was analyzed to see how certain variables changed with respect to each other. Plus, an analysis of correlation between variables was done, especially to see if any linear relationships existed. Finally, an analysis of mean free path and expected number of returns with respect to rainfall rate was accomplished.

Previous weather research on this system was accomplished in 1996 by Captain Clifton Stargardt (Stargardt 1996). However, the ladar system has been improved since the completion of his work, so comparisons between his results and the ones seen in this thesis were not able to be done. In any case, Captain Stargardt's work was instrumental in defining the framework of some portions of this thesis.

1.4 - Limitations

Limitations existed in three areas within the thesis research. First, the type, intensity, and duration of the weather events were out of our control. Second, no particle size distribution data, either fog or raindrop, was available. And third, all the laser radar images contained the target panel as the target.

1.5 - Overview

Chapter 2 incorporates background work and theory concerning the use of laser radar and radiative transfer through the atmosphere, as well as information about mean free path. Chapter 3 outlines the procedure used to collect and organize the data for the analysis. Chapter 4 explains the results of the analysis of the data. Chapter 5 summarizes the work done in this thesis and offers recommendations and suggestions for future work.

II. Background

2.1 - Mie Scattering Theory

When determining which scattering theory to use, the value of the size parameter x $\left(x = \frac{2\pi r}{\lambda} \right)$ needs to be known, where r is particle radius and λ is wavelength. The size parameter relates the size of the scatterer to the wavelength of the incident radiation. Since a 1.06- μm laser is of relevance here and our scatterers (fog, haze, and rain droplets) are about the same size, the size parameter is close to and larger than one. When this is the case, Mie theory is used to explain our scattering characteristics. Many different authors address Mie scattering theory; however the work of Thomas Kyle in his 1991 book was chosen for this thesis.

Mie scattering theory is the result of solving the Maxwell equations for the interaction of an electromagnetic wave with a spherical particle. Mie theory takes absorption into account; furthermore, the particle is assumed to have a refractive index m , which may be real or complex. The most important approximation that is built into Mie theory is that particles are assumed to be spheres. This is used so that complex-shaped aerosols can be considered to be a distribution of different sized spheres.

Several concepts are important to the understanding of scattering within the Mie regime. Extinction efficiency, Q_{ext} , is defined as the energy removed from the incident beam divided by the geometric cross section of the scatterer

$$Q_{ext} = \frac{2}{x^2} \sum_{n=1}^{\infty} (2n + 1) \operatorname{Re}(a_n + b_n)$$
$$\sigma_{ext} = \pi r^2 Q_{ext}$$

where r is the radius of the scattering particle, σ_{ext} is the extinction cross section, and a_n and b_n are the expansion parameters of Maxwell's equations. The efficiency is the factor by which the actual geometric cross section must be magnified or diminished to produce the observed extinction. The scattering efficiency, \mathcal{Q}_{sct} , is the area of the incident beam that appears to have been scattered divided by the geometric cross sectional area of the scatterer.

$$\mathcal{Q}_{sct} = \frac{2}{x^2} \sum (2n + 1)(|a_n|^2 + |b_n|^2)$$

$$\sigma_{sct} = \pi r^2 \mathcal{Q}_{sct}$$

Finally, the absorption efficiency is the difference between the extinction efficiency and the scattering efficiency, since these quantities are directly related.

$$\mathcal{Q}_{abs} = \mathcal{Q}_{ext} - \mathcal{Q}_{sct}$$

$$\sigma_{abs} = \sigma_{ext} - \sigma_{sct}$$

Since efficiency times geometric cross section equals cross section, we can draw some conclusions about the relationship between particle size and efficiency. For small x , efficiencies are almost zero. This means that the particles scatter much less radiation than their geometric cross section would suggest. However, as x increases, the efficiencies also increase. So for non-absorbing particles, the efficiencies, both extinction and scattering, asymptotically approach a value of two.

2.2 - Attenuation Due to Fog

2.2.1 - Chylek - 1978

In his 1978 paper, Petr Chylek showed for the first time that a relationship existed, at a certain wavelength, between the volume extinction coefficient k and the liquid water content (LWC) W which was independent of drop size distribution. By assuming spherical droplets with a size distribution of $n(r)$ (r was radius) per unit volume, relations for LWC and extinction coefficient were

$$W = \frac{4}{3} \pi \rho \int r^3 n(r) dr \quad (1)$$

$$k(\lambda) = \int \sigma_{ext}(\lambda, r) n(r) dr \quad (2)$$

where ρ was water density, λ was the wavelength of the radiation, and $\sigma_{ext}(\lambda, r)$ was the extinction cross section of a spherical droplet of radius r at wavelength λ . When a normalized cross section, $Q_{ext}(\lambda, r) = \frac{\sigma_{ext}(\lambda, r)}{\pi r^2}$, was used in place of extinction cross section, the equation for k became

$$k(\lambda) = \pi \int Q_{ext}(\lambda, r) r^2 n(r) dr \quad (4)$$

and a relation between W and k could be determined

$$W = \frac{4\rho}{3} \frac{\int r^3 n(r) dr}{\int Q_{ext}(\lambda, r) r^2 n(r) dr} k(\lambda) \quad (5)$$

At this point, it seemed that only an approximate relationship between W and k , independent of $n(r)$, could be determined since Q_{ext} was a very complicated quantity.

Chylek then began to determine an empirical relationship between W and k . After failing with several other relationships, a linear relation, $Q_{ext}(x) = cx$, was used, where c

was the slope, and x was the size parameter $\left(x = \frac{2\pi r}{\lambda} \right)$. This approximation overestimated Q_{ext} values at some values of x and underestimated it at other values. These two errors tended to cancel each other in the integral; therefore, this linear relation looked fairly accurate. When $Q_{ext} = cx$ was substituted into (4) for Q_{ext} , then both (4) and (1) had a $\int r^3 n(r) dr$ term, so this term canceled, eliminating the dependence on size distribution.

This left

$$W = \frac{2\rho \lambda k}{3\pi c}$$

a linear relationship between W and k , independent of $n(r)$.

Using over 300 different size distributions, Chylek calculated W and k for different wavelengths. He saw a strong linear relation at 11 μm that was not true at any other wavelength. All the points fell reasonably close to the $k = 128W$ line. Overall, for large LWC, the agreement between the line and the points was excellent. The errors canceled since at this point all drop sizes up to maximum size parameter x_M $\left(x_M = \frac{2\pi r_M}{\lambda} \right)$ had been considered. On the other hand, at low LWC values, the line did not fit the data very well since $x \ll x_M$, and the integration had not canceled the errors yet.

2.2.2 - Pinnick, et al. - 1978

Pinnick, et al. set out to make measurements of the size distribution of fog and haze. Nineteen vertical profiles of the structure of size distribution and number concentration for fog and haze were made near Grafenwöhr, Germany in February 1976. It was assumed that the fog and haze were composed of liquid water droplets.

Linear relations were found to exist between W and k once again. Similar to the results found by Chylek, Pinnick et al. found a linear relation at 10 μm . However, they also discovered highly linear relations at 0.55, 1.20, and 4.0 μm . The authors derived empirical relations between W and k and compared their results to those done by Eldridge (1966, 1971), Barteneva and Polyakova (1965), and Kumai (1973). Values of LWC ended up varying by at least an order of magnitude, and this difference was attributed to the widely differing fog droplet size distributions measured by the other authors.

2.2.3 - Pinnick, et al. - 1979

In this study, the authors set out to verify the relations between W and k by calculating the values for 341 different fog droplet size distributions measured under various meteorological situations. In previous works, linear relations were determined to exist between W and k at 11 μm , but in this case, a linear relation was found to exist between absorption and W at 3.8 and 9.5 μm .

The linear equation $Q_{\text{ext}} = cx$ was tested at 0.55, 1.2, 4.0, and 11.0 μm . Results were positive at 11 μm , reaffirming the work of Pinnick (Pinnick 1978) and Chylek (Chylek 1978); however, the relation failed for 0.55 μm . So at this wavelength, no size-distribution-independent relation between W and k existed. It was determined that as wavelength increased the $Q_{\text{ext}} = cx$ relation was appropriate for the larger drop radii in the sample.

Differences in fog content and fog type were examined in this study. It was found that contaminants in the water fog drops did not affect the refractive indices of the fog, because the volume fraction of contaminant was too small when compared to the volume

fraction of water in the drop. Also, similar $Q_{ext} = cx$ results were found when the fogs were divided into radiation and advection fogs—though this relation worked better for radiation fogs.

2.2.4 - Tonna - 1991

In 1991, Glauco Tonna studied the behavior of the relationships between volume backscattering coefficient β and volume extinction coefficient σ , liquid water content W and σ , and $\sigma(0.55 \mu\text{m})$ and σ for 40 wavelengths in the $\lambda = 0.25\text{-}12 \mu\text{m}$ range. He considered 239 experimental size spectra of valley, advection, and radiation fogs with droplet radii ranging from 0.3 to 54 μm . This study was of particular interest since Tonna gave specific results for a 1.06- μm Nd:YAG laser, which was the laser of interest in this thesis project.

At each droplet radius distribution $n(r)$ and each wavelength, volume extinction coefficient and volume backscattering coefficient were computed. The following relations were used

$$\sigma(\lambda) = \int_{r_m}^{r_M} \pi r^2 K[r, m(\lambda)] n(r) dr$$

$$\beta(\lambda) = \frac{\lambda^2}{4\pi^2} \int_{r_m}^{r_M} \frac{i_1[\pi, r, m(\lambda)] + i_2[\pi, r, m(\lambda)]}{2} n(r) dr$$

where r_m and r_M were the lower and upper radii of the $n(r)$ considered, K was the efficiency factor for extinction, $m(\lambda)$ was the complex refractive index of water and i_1 and i_2 were the Mie intensity functions for backscattered light.

The data elaboration consisted of three steps. First, the average β and σ and the relevant dispersion coefficient (equal to the standard deviation over the mean value in percent) were determined at each wavelength. Second, the data points were fitted with power law relations ($y = cx^K$), and the correlation and dispersion coefficients were defined. Third, the data points were fitted with a straight line, and the relative differences between the correlation and dispersion were computed between the non-linear and linear fits.

Tonna then looked at the β - σ , W - σ , and $\sigma(0.55 \mu\text{m})$ - σ power law relations individually. The $1.06 \mu\text{m}$ information is presented here. The β - σ relation was $\beta = c_1 \sigma^{K1}$, where $c_1 = 0.03584$ and $K1 = 0.903$. The correlation coefficient was 0.962, and the dispersion coefficient was 18.25%. Good accuracy in the fitted curve appeared in this case. The W - σ relation was $W = c_2 \sigma^{K2}$, where $c_2 = 3.223$ and $K2 = 0.838$. For this case, the correlation and dispersion coefficients had values of 0.863 and 34.56% respectively. The accuracy for this curve was not as good as the previous relation. Finally, the $\sigma(0.55 \mu\text{m})$ - σ relation was determined from $\sigma(0.55 \mu\text{m}) = c_3 \sigma^{K3}$. The information for this case could not be obtained directly, so a short series of calculations was performed. A formula for visibility V was used where:

$$V = \frac{3.912}{\sigma(0.55 \mu\text{m})}$$

and $\sigma(0.55 \mu\text{m}) = a_3 \sigma$. For $1.06 \mu\text{m}$, $a_3 = 0.979$; therefore,

$$V = \frac{3.996}{\sigma}$$

with a correlation of 0.999 and a dispersion of 3.39%.

Finally, Tonna completed a comparison between non-linear and linear fitting for the data points. Overall, the use of a power-law relation produced an increase in correlation of 23% and a decrease in dispersion of 6%. Specifically for the β - σ case, mean values of the relative differences in correlation and dispersion were 3.8% and -2.6% respectively. For the W - σ case, the mean values were 6.5% and -2.1%, and for the $\sigma(0.55 \mu\text{m})$ - σ case, mean values were 1.3% and -1.4%, small improvements when compared to the other fits. Overall, Tonna found that the power law relation worked much better than a linear relation.

2.3 - Attenuation by Rain

2.3.1 - Jelalian - 1992

In his 1992 book, Albert Jelalian examined the atmospheric effects on laser radar systems. Limited information was given on attenuation by haze, fog, and rain. Information was given for 1.06- μm lasers with no indication as to how the data was collected or even determined.

In one table, the author illustrated the amount of attenuation as a function of laser wavelength. For a 1.06- μm laser, a light haze resulted in 1.5-dB/km attenuation while a haze with 3 km visibility caused 3.9-dB/km attenuation. Also, lower visibilities or higher rainfall rates produced the same attenuations at longer wavelengths as seen at 1.06 μm . Overall, a 12.5-mm/hr rainfall (classified by the author as a medium rain) caused 5.5-dB/km of attenuation for wavelengths between 0.7 μm and 0.3 cm.

Later in the book, an equation relating attenuation and rainfall rate was given

$$\alpha = 0.29 + \frac{R}{2.53} - \left(\frac{R}{20.3} \right)^2$$

where α was attenuation in dB/km and R was rainfall rate in mm/hr. When a 12.5-mm/hr rainfall rate was used in this formula, an attenuation of 4.85 dB/km resulted. This differed from the 5.5 dB/km that was read before from the table. This difference could be due to the fact that the above formula and table could have been produced from two differing studies with dissimilar test conditions.

Finally, Jelalian showed range performance, as a function of atmospheric conditions, at a 1-m² target for a 1.06-μm laser. In a light haze, the target was detectable at 9 km. This range decreased to 7.5 km in a 4-mm/hr rainfall. When the rainfall rate increased to 20-mm/hr, the target range dropped considerably to about 3 km. This data gave an indication of how the laser performed under varying weather conditions. However, Jelalian never defined the conditions for detecting the target.

2.4 - Mean Free Path

2.4.1 - Sears and Salinger - 1975

As molecules move through the atmosphere, they collide with other molecules. These collisions cause a molecule to move in an irregular, zigzag path. The ladar system detects collisions between the laser and the hydrometeors as false returns. But how do you determine how far the laser beam travels before it experiences its first collision with a fog or rain droplet? This is found by calculating the mean free path of the laser. Since

only the center-to-center distance determines whether a collision takes place, we can shrink the bullet laser to a point, so the target droplet then occupies the sphere of exclusion with radius d . A collision between a bullet and a target occurs whenever the distance between the centers becomes equal to the droplet diameter d . In this thesis, the bullet is the laser, and the target molecules are the fog or rain droplets encountered on the laser test range.

To derive an expression for mean free path for a distribution of particles, we first need to state several things. First, consider a thin layer of gas of dimensions L , L , and Δx where

$$\begin{aligned} L &= \text{dimension of layer} \\ \Delta x &= \text{thickness of layer} \end{aligned}$$

So the volume of this layer is $L^2 \Delta x$. Then, a very large number N of bullet photons from the laser move toward the layer which contains a number n of smaller target droplets per unit volume, each with radius d . The area of a single target droplet is

$$\sigma = \pi d^2$$

Since we are dealing with a drop distribution, the formula for total droplet target area is

$$L^2 \Delta x \sum_i \sigma_i n_i \quad (1)$$

The first two terms corresponds to the layer, and the summation factor represents the distribution of target particles.

Some bullet photons from the laser collide with the target droplets. The ratio of the number of collisions, ΔN , to the total number of bullets, N , equals the ratio of the area presented by the target droplets to the total area presented by the layer

$$\frac{\Delta N}{N} = \frac{\text{droplet area}}{\text{total area}}$$

Since the total droplet area is $L^2 \Delta x \sum_i \sigma_i n_i$ and the total area of the layer face is L^2 ,

$$\frac{\Delta N}{N} = \frac{L^2 \Delta x \sum_i \sigma_i n_i}{L^2} = \Delta x \sum_i \sigma_i n_i \quad (2)$$

Next, we introduce the concept of the survival equation. This equation identifies how many molecules out of an initial number have not yet made a collision after traveling a certain distance Δx . So, interpret ΔN as the decrease in the number N

$$\frac{\Delta N}{N} = -\Delta x \sum_i \sigma_i n_i \quad (3)$$

where a negative sign is inserted to reflect the decrease in N . If we assume that N decreases continuously by x , with a large N , then

$$\frac{dN}{N} = -dx \sum_i \sigma_i n_i$$

If $N = N_0$ at $x = 0$, then through integration

$$N = N_0 \exp(-x \sum_i \sigma_i n_i) \quad (4)$$

which is the survival equation. Inserting this expression into (2), we obtain

$$\Delta N = N_0 \exp(-x \sum_i \sigma_i n_i) \Delta x \sum_i \sigma_i n_i \quad (5)$$

So, we are looking for a number of false returns in a ladar image, depending on the number and size of water particles in the atmosphere.

Finally, we come to the concept of mean free path. Mean free path, l , is interpreted as the average distance traveled by a group of molecules before it makes its

first collision. To calculate it, multiply x by the number of particles ΔN that travel the distance x before colliding, sum over all x , and divide by the total number N_o .

$$l = \frac{\sum_j x_j \Delta N}{N_o} = \sum_j x_j \exp(-x \sum_i \sigma_i n_i) \Delta x \sum_i \sigma_i n_i$$

Replacing the sum over j by an integral over all j and Δx , we have

$$l = \sum_i \sigma_i n_i \int_0^\infty x \exp(-x \sum_i \sigma_i n_i) dx \quad (6)$$

We need to evaluate the integral $\int_0^\infty x \exp\left(-x \sum_i \sigma_i n_i\right) dx$. Expanding the sum inside the integral, we see

$$\int_0^\infty x \exp(-x \sum_i \sigma_i n_i) dx = \int_0^\infty x \exp(-x \sigma_1 n_1) \exp(-x \sigma_2 n_2) \exp(-x \sigma_3 n_3) \dots dx$$

This integral cannot be solved analytically, so a numerical solution needs to approximate this integral. We return to the sum seen above and use this sum instead of an integral.

$$\sum_j x_j \exp(-x_j \sum_i \sigma_i n_i) dx \quad (7)$$

When (7) is substituted into (6) for the integral, the equation for mean free path becomes

$$\sum_i \sigma_i n_i \sum_j x_j \exp(-x_j \sum_i \sigma_i n_i) dx \quad (8)$$

The sums, evaluated over a large interval of sizes and number distributions, provide a very close approximation to the value of the full mean free path equation. In this thesis, $i = 60$ and $j = 100000$. These values were chosen to ensure that enough values were included in the sum to make it approximate the integral.

This concludes the summary of background material on the performance of the laser radar in varying weather regimes, namely fog and rain, and the theory of mean free path.

III. Procedure

3.1 - Image Analysis

A neodymium yttrium aluminum garnet (Nd:YAG) pulsed laser creates the ladar images used in this thesis. The beam diameter is 2.0 cm with a 0.07-mrad spread, and the power per pulse is 2000 W. The minimum detectable power (power needed to register a return) is about 72 nW (assuming S/N of eight), found by dividing the threshold voltage by responsivity. The laser has a pulse width of 12 ns and a pulse rate frequency of 10 kHz; the system operates at a sampling rate of 1 GHz. The system also is capable of discriminating from background noise by using a correlation technique on the return signals. The system looks for a return pulse 12 ns long, so a return of any other length is discarded.

Labview, an image analysis program with graphical programming capabilities, was used to analyze the laser radar images. A laser radar image file is opened, and a magnification box is placed around a portion of the image to run the program. This allows the analysis to be focused on the target area in question. Two programs are used within the Labview environment: one to count false returns and one to count dropouts on the user specified region of the laser radar images. The first, *Falsrtn.vi*, counts the number of false return pixels within a portion of open sky. A portion of open sky is used since no returns are expected from it—no specified targets unlike those used when running *Dropout.vi*. *Dropout.vi*, the second program, counts the number of dropout pixels. This permits the user to see whether a return comes from the target or an obstruction in front of the target, such as a raindrop. *Falsrtn.vi* determines the total number of false returns,

the mean value of their distances, standard deviation of distance, variance of distance, and percentage of the picture that is false returns; however, *Dropout.vi* only computes total number and percentage since a dropout is recorded as a “zero.” So the mean, standard deviation, and variance of a list of zeros is zero. This data is then written into a spreadsheet file. The same spreadsheet saves the data from multiple images on a particular day, creating a file organized for time series analysis.

Quality control of the images is crucial. Two types of erroneous images appeared in this analysis. First, the image could be “washed out”, allowing for no identification of targets or borders between objects and sky. Second, portions of the image could be “blacked out.” This made it difficult to determine whether this area of returns came from atmospheric particles or an error with the system. Also, any images where an appropriately sized area for analysis was not able to be produced were discarded. This was due to changes in the direction of aim of the laser radar. Out of all images, less than ten percent were discarded for the above listed reasons.

A defect appeared on the laser’s telescopic lens in September 1997. The defect appeared as a circular region of returns within the laser image. The laser operators determined that one of the interior lenses of the telescopic lens had some sort of contamination on it, and they were unable to remove and clean this lens. Some preliminary analysis was done in Labview using the defective images to see how the defect affected the images and what type of returns it produced. However, since the behavior of the laser with a defective lens was not the focus of this thesis, I discontinued the analysis of these images and concentrated on images created before the defect appeared.

When running *Dropout.vi*, the target panel on the range was used. This panel, one of a pair, is located 500 m downrange from the laser. *Dropout.vi* was run on each day. Since the panel is rectangular, the magnification area fit the panel almost exactly. The size of the panel ranged from 15040 pixels to 15485 pixels, due to changes in the aiming angle of the laser. However, the number of pixels used on the 27th was smaller since the data was processed by the scientists at Eglin. Table 3.1 lists the total pixels for each day.

Date	Pixels
3-Jan-97	15066
19-Feb-97	15066
24-Feb-97	15485
25-Feb-97	15390
26-Feb-97	15040
27-Feb-97	7000
28-Feb-97	15040

Table 3.1: Total number of pixels for the target panel on each of the seven days in question

When running *Falsrtn.vi*, a portion of open sky was used as the analysis area. An area with approximately 16,500 pixels was used each day—the size varying by how much open sky was available in each image. Table 3.2 lists the number of pixels used for each day.

Date	Pixels
3-Jan-97	16470
19-Feb-97	16510
24-Feb-97	16506
25-Feb-97	16506
26-Feb-97	16240
27-Feb-97	10000
28-Feb-97	16500

Table 3.2: Total number pixels used for the portion of open sky during the false return analysis

3.2 - Instrumentation

The weather station is located 500 m from the ladar, and its instruments measure rainfall rate, visibility, particle size, raindrop size, and other meteorological variables such as temperature, relative humidity, pressure, wind speed, and wind direction.

Rainfall rate is determined by Scientific Technology's Model ORG-705 optical Precipitation Gauge. The sensor evaluates rainfall by detecting the optical irregularities induced within the sample volume by precipitation particles falling through a beam of partially coherent infrared light. The light source is an infrared light emitting diode, and the intensity of the scintillations of this light, caused by the raindrops passing though the beam, determines the rainfall rate. The gauge reports a voltage which can be converted to a rainfall rate by

$$R = 10^{(V-0.65)}$$

where R is rainfall rate in mm/hr and V is voltage in volts. Calibration of the instrument is based on the Marshall-Palmer drop size distribution for natural rain events. The system is accurate to 1% from 10 mm/hr to 100 mm/hr and to 4% elsewhere and includes a measurement range of 0.1 to 1000 mm/hr (Metvan Instrumentation).

Visibility is measured by the Model 8360 Forward Scatter Visibility Sensor. A beam of radiation, 950-nm, illuminates a volume of atmosphere, and the energy scattered by the interaction of the beam with particles in the atmosphere is measured at a scatter angle of 35 degrees. This angle is used since it provides a linear scattered signal amplitude for the particle size distribution of interest, either haze, fog, rain, or snow. The sensor eliminates error at the optical detector by using a measurement method that does not depend upon an absolute calibration. A pair of emitters are used in conjunction with a pair

of detectors. The facing emitter/detector pair measures the direct transmission through the volume while the pair at a 35 degree angle measures the energy scattered by the atmospheric particles. This setup allows for calculations of an absolute extinction coefficient independent of contaminants upon the optical surfaces or the effects of temperature changes on the optical source and measurement electronics. The sensor determines visibilities ranging from 160 m to 32 km (Metvan Instrumentation).

A Classical Scattering Aerosol Spectrometer Probe (CSASP) is used to measure fog droplet size distributions. The probe sizes the drops into 4 subranges with a useful range of 0.3 μm to 20 μm . Minimum detectable size is 0.3 μm with a size resolution of 0.03 μm . The subranges are 0.3-0.75 μm , 0.5-2.75 μm , 1.0-12.5 μm , and 2.0-20.0 μm . Each subrange can then be divided into 15 size channels or bins. A 5-mW He-Ne high order multi-mode laser illuminates a sample area of 0.018 mm^2 at 10 \times magnification (Metvan Instrumentation).

Raindrop sizes are determined by the Ground Based Precipitation Probe. Operating as a spectrometer probe, the device outputs particle diameters in binary code. The system can provide 62 size channels with a size range of 0.2 to 12.4 mm. A He-Ne laser illuminates the particles and images them as shadowgraphs onto a photodiode array. The number of elements shadowed by the particle determines particle size. Size resolution is 200 μm with a minimum detectable size of 142 μm (Metvan Instrumentation).

Both the CSASP and the Precipitation Probe failed to produce any data for this project. So when particle size data was needed for the mean free path analysis, a Marshall-Palmer distribution was assumed for the rain drops.

3.3 - Meteorological Data

Meteorological information is also recorded when the images are produced. A computer connected to the weather station records the data every minute, and this information is saved in ASCII file format. Rainfall rate data is recorded separately since it must be converted from volts. Spreadsheets easily open the weather data files; therefore, the Labview spreadsheet data files easily merge with the weather data files. Since radar images are not produced every minute, extra work needed to be done to match the right weather data with the image. An example of a portion of a completed worksheet is given in Table 3.3.

3.4 - Data and Graphical Analysis

Once Labview calculated all the numbers for the images and the weather data was married with this data, analysis of this data began. All data was transferred from the spreadsheets into a mathematics program to make future calculations and graphing simpler. Five more tasks were performed with the data. First, extinction coefficient β was calculated. Second, the correlation coefficients between several different variables were determined. Third, several graphs were made to display relationships between variables. Fourth, control charts displayed the behavior of the system during the weather events. And fifth, for the days when rain was present, an analysis of mean free path and the survival equation was accomplished.

Data on false returns for 19 Feb				254x65 pixels				Wx for 19 Feb-97			
Image	Std. Dev.	mean	variance	#	%	Time	RR (volts)	RR (mm/hr)	Vis (km)		
3	27.461	502.931	804.402	16	0.097	1624	0	0.224	32.4		
4	53.496	514.35	2976.33	26	0.157	1627	0	0.224	32.41		
5	34.049	513.771	1217.31	21	0.127	1629	0	0.224	32.42		
6	50.242	501.685	2638.98	23	0.139	1630	0	0.224	32.4		
7	42.483	503.859	1925.11	16	0.097	1632	0	0.224	32.42		
8	28.184	494.13	836.161	20	0.121	1633	0	0.224	32.41		
9	30.503	515.783	963.65	29	0.176	1633	0	0.224	32.41		
10	34.98	508.566	1305.15	16	0.097	1634	0	0.224	32.38		
11	0	489.3	0	1	0.006	1635	0	0.224	32.41		
12	0	491.85	0	1	0.006	1636	0	0.224	32.42		
13	6.935	478.35	64.125	4	0.024	1637	0	0.224	32.38		
14	6.935	478.35	64.125	4	0.024	1641	0	0.224	32.4		
15	6.935	478.35	64.125	4	0.024	1642	0	0.224	32.41		
16	8.7	484.35	151.38	2	0.012	1644	0	0.224	32.42		
17	0	472.65	0	1	0.006	1645	0	0.224	32.38		
18	0	492.9	0	1	0.006	1646	0	0.224	32.42		

Table 3.3 - Example spreadsheet file used in organizing the data sets for each day

3.4.1 - Data Analysis

Two additional calculations were performed on the data. The first was the calculation of an extinction coefficient, β_{ext} . Extinction incorporates the sum of absorption and scattering, so extinction measures the total disruption of the beam of light by the atmosphere (Huschke 1959). The calculation of β_{ext} was done using a version of Koschmeider's Law.

$$\beta_{ext} = \frac{3.912}{Visibility}$$

This formula, simple in nature, allows the calculation of extinction to be made directly from the visibility. The second calculation done on the data was the determination of correlation coefficients. Given n pairs of observations (x_n, y_n) , a relationship between x and y can be determined. The correlation coefficient for the n pairs is

$$r = \frac{\left(n \sum_i x_i y_i \right) - \left(\sum_i x_i \right) \left(\sum_i y_i \right)}{\sqrt{\left(n \sum_i x_i^2 \right) - \left(\sum_i x_i \right)^2} \sqrt{\left(n \sum_i y_i^2 \right) - \left(\sum_i y_i \right)^2}}$$

The correlation coefficient r has several important properties. First, the value of r does not depend on which of the two variables under study is labeled x and which is labeled y . Second, the value of r is independent of the units in which x and y are measured. Third, the value of r falls between positive and negative one, $-1 \leq r \leq 1$. So an r of positive one corresponds to the largest possible positive relationship, and an r of negative one identifies the largest possible negative relationship. And fourth, $r = 1$ if and only if all (x_n, y_n) pairs lie on a straight line with positive slope, and $r = -1$ if and only if all pairs lie on a straight line with negative slope. The correlation coefficient measures the degree of

linear relationship among variables; a value near zero is not evidence of the lack of a strong relationship, just the absence of a linear one. Correlation is said to be weak when $0 \leq |r| \leq 0.5$, strong if $0.8 \leq |r| \leq 1$, and moderate otherwise (Devore 1995).

3.4.2 - Graphical Analysis

The spreadsheet program was used to make graphing of the variables simpler and more efficient. Several different graphs were produced to show the relations between the variables and the behavior of those variables individually. Graphs of particular interest were those showing the behavior of the dropouts and false returns with varying rainfall rate and visibility, since these graphs showed the performance of the system as the weather conditions changed.

3.4.3 - Control Charts

Control charts are a statistical tool used to determine whether a process is in statistical control. Donald Wheeler and David Chambers, in their 1992 textbook, use Walter Shewhart's 1986 definition of statistical control—"a phenomenon. . . (for which) through the use of past experience, we can predict, at least within limits, how the phenomenon may be expected to behave in the future." Instead of seeking a theoretical model for data obtained from some well-defined phenomenon, the control chart seeks to determine if a sequence of data may be used for predictions of what will occur in the future. The control chart is an inductive tool—involving extrapolation from specific observations back to general principles. Weather significantly affects the performance of the laser radar system, and control charts quickly and effectively show this point.

In this thesis, the subgroup used in the control chart has a size $n = 1$. So, a special case needed to be employed to create the chart. The charts were created using the individual values and the moving range (difference between two successive values). These values were then used to calculate the 3-sigma limits for the individual values and the moving range using the formulas:

$$\begin{aligned} CL_X &= \bar{X} \\ CL_R &= mR \\ UNPL_X &= \bar{X} + 2.660mR \\ LNPL_X &= \bar{X} - 2.660mR \\ UCL_R &= 3.28mR \end{aligned}$$

$$\begin{aligned} CL_X &= \text{mean of sample } X = \bar{X} \\ CL_R &= \text{mean of moving range } R = mR \\ UNPL_X &= \text{upper control limit of sample } X \\ LNPL_X &= \text{lower control limit of sample } X \\ UCL_R &= \text{upper control limit of moving range } R \end{aligned}$$

Any lower control limit less than zero is set to zero.

“Run tests” determine patterns within a record illustrated by a control chart. A “run” of points about the central line (the mean) consists of a group of successive points that are all on the same side of the central line. For example, a run of length two consists of two points on the same side of the central line. When several consecutive points fall on the same side of the central line, this may be interpreted as a shift in the behavior of the process. A run indicates whether a special influence is operating, meaning that something beyond normal randomness of the system affects the performance.

Four rules have been established for defining a lack of control within a process. One, a lack of control is indicated whenever a single point falls outside the 3-sigma control limits. Two, a lack of control is indicated whenever at least two out of three successive

values fall on the same side of, and more than two sigma units away from, the central line. Three, a lack of control is indicated whenever at least four out of five successive values fall on the same side of, and more than one sigma unit away from, the central line. And four, a lack of control is indicated whenever at least eight successive values fall on the same side of the central line.

3.4.4 - Mean Free Path and Survival Equation

The concepts of mean free path and survival equation were introduced into this thesis to perform an analysis of the false returns seen in the images. Mean free path is directly related to rain rate, so the two days with rain provide an opportunity to see how the system performs in this type of weather. Mean free path and the survival equation together help in describing the atmospheric propagation of the laser, the size of the drops encountered by the laser, and the number of false returns expected in a ladar image. Therefore, by considering mean free path and the survival equation, we are able to look at the images from a different angle by asking several key questions. Can the atmosphere be described in another manner according to the mean free path? What size drops are causing the false returns we see in the images? These issues were tackled in this section of the research.

Mean free path was calculated assuming a Marshall-Palmer drop size distribution. In Chapter-2, an equation was derived which used all particle sizes, number densities, and distances to determine a mean free path for a particular rainfall rate. A particular rainfall rate, when used in these equations, produced a mean free path.

$$mfp = \sum_{i=0}^{50} \sigma l_i n l_i \sum_{j=0}^{100000} x_j \exp(-x_j \sum_{i=0}^{50} \sigma l_i n l_i) dx$$

This mean free path was then used in the survival equation. The survival equation was used to compute the expected number of returns for the mean free path. When the mean free path was inserted into the survival equation, the number of expected false returns was computed. Now, one could see the number of false returns for the corresponding mean free path and rainfall rate.

$$\Delta N = N_0 \frac{1}{mfp} \exp\left(-\frac{dis}{mfp}\right) deldis$$

where

$$N_0 = 16000 \text{ m}^{-3}$$

$$dis = 500 \text{ m}$$

$$deldis = 100 \text{ m}$$

By looking at mean free path, we are able to better explain why false returns happen.

Raindrops in the air intercept the laser beam, and by looking at the mean free path of the laser beam in the atmosphere, we can acquire a better understanding of the sizes of the raindrops causing the false returns.

The final step in this portion of the thesis work involved determining a minimum drop diameter. We were concerned with the size of the drops that caused the false returns seen in the lidar images. Once this minimum diameter of concern was determined, then it would be known that drops of this size and larger caused the false returns. To determine this critical diameter, the equation employed to compute the mean free path was used again. Then the mean free path was used to compute the number of false returns, using the survival equation. A critical diameter was randomly chosen to be the initial guess, and

after this, the better match minimum diameter was found through regression. When the correct minimum diameter was found, the number of false returns calculated with the survival equation was of the same order of magnitude as the number of false returns seen in the images on a particular day.

IV. Results

4.1 - Correlation Coefficients Between Several Variables

Correlation coefficients were calculated for each day for several combinations of parameters and weather variables, whenever possible. Table 4.1 shows the correlation between dropout percentage and visibility, and Table 4.2 shows the correlation between dropout percentage and rain rate. Table 4.3 shows the correlation between false return percentage and visibility while Table 4.4 shows the correlation between false return percentage and rain rate. The days when there was no rain have N/A in their block. Table 4.5 shows the correlation between extinction coefficient β and number of dropouts. On some days, we see strong linear relationships between variables while on other days the relationship is strongly not linear. Overall, the strongest linear relationships were seen between dropout percentage and visibility or rain rate. The relationships between false return percentage and the weather were not strongly linear. It is tough to draw conclusions about the relationships between the variables for two reasons. One, on most of the days, the number of data points was fairly small, weakening the statistical relationships. And two, the weather was never too severe on any day studied here, especially during the rain days. It was expected that light rain or high visibility situations would not affect the performance of the system significantly, and this may be a reason why the correlation coefficients are not consistent throughout all the days.

Table 4.1

Date	% drop/vis
3-Jan	-0.403
19-Feb	-0.168
24-Feb	-0.898
25-Feb	0.567
26-Feb	-0.791
27-Feb	-0.191
28-Feb	0.23

Table 4.2

Date	% drop/RR
3-Jan	N/A
19-Feb	N/A
24-Feb	0.848
25-Feb	-0.784
26-Feb	N/A
27-Feb	N/A
28-Feb	N/A

Table 4.3

Date	% fr / vis
3-Jan	0.611
19-Feb	-0.044
24-Feb	-0.267
25-Feb	-0.751
26-Feb	0.377
27-Feb	-0.245
28-Feb	0.106

Table 4.4

Date	% fr / RR
3-Jan	N/A
19-Feb	N/A
24-Feb	0.276
25-Feb	-0.131
26-Feb	N/A
27-Feb	N/A
28-Feb	N/A

Table 4.5

Date	β / drop
3-Jan	0.28
19-Feb	0.167
24-Feb	0.892
25-Feb	-0.502
26-Feb	0.861
27-Feb	0.254
28-Feb	-0.213

Tables 4.1 through 4.5 - Correlation coefficients between percent dropouts (% drop) and visibility (vis) and , percent dropout and rainfall rate (RR), percent false returns (% fr) and visibility, percent false returns and rainfall rate, and extinction coefficient (β) and number of dropouts (drop)

4.2 - Graphical Analysis of Variables

Graphical representation of the image degradation is extremely helpful in understanding the behavior of the laser system as the weather varies. Particularly, the number of dropouts or false returns registered identifies the level of degradation caused by the weather. The following six sections highlight the behavior of the system, graphically, with certain parameters in mind. A combination graph, showing dropouts or false returns plotted with visibility or rain rate versus time, shows a better overall view of the performance on a given day. Dropouts and false returns are plotted against visibility and rain rate; extinction, as calculated from the visibility, is plotted against time. In some cases, the range on either the *x* or *y* axis was changed in order to spread out clustered data points. This should be kept in mind when a comparison of two graphs is being made.

4.2.1 - Dropouts and Visibility vs. Time

The following seven graphs give an overall picture of the behavior of the dropouts with time, as well as an indication of how the visibility was changing over that time. Figures 4.1 - 4.7 represent January 3rd and February 19th, 24th, 25th, 26th, 27th, and 28th, respectively.

Number of dropouts, Visibility vs. Time

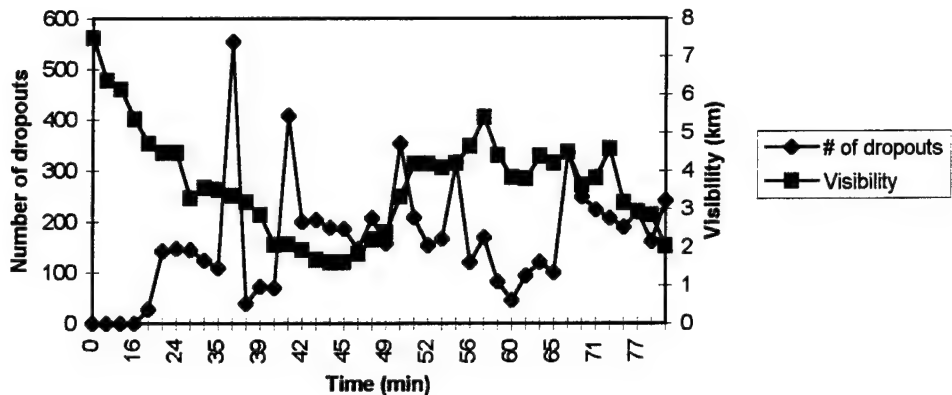


Figure 4.1 - Number of dropouts and visibility changing with respect to time on January 3, 1997. Number of dropouts remains within the same order of magnitude as the visibility decreases.

Number of dropouts, Visibility vs. Time

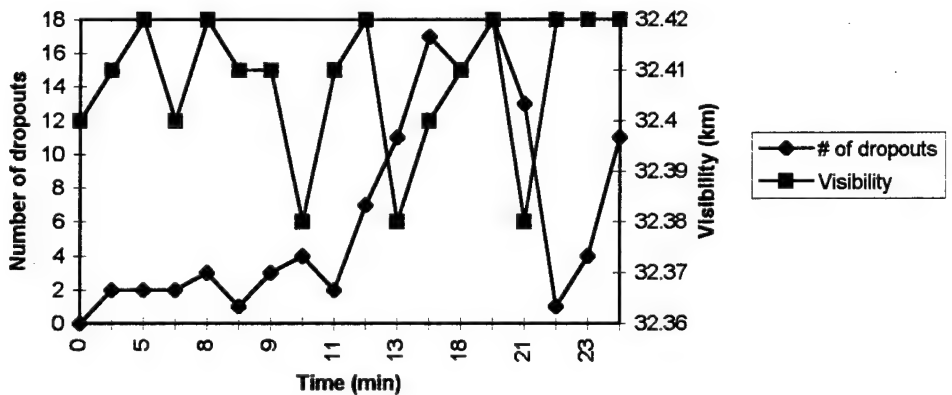


Figure 4.2 - Number of dropouts and visibility changing with respect to time on February 19, 1997. On this day, visibility remained very constant, so the number of dropouts did not change much.

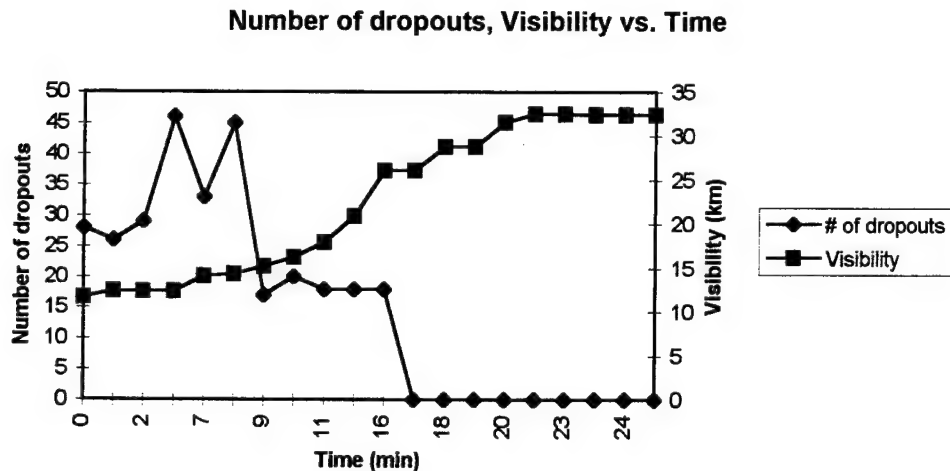


Figure 4.3 - Number of dropouts and visibility changing with respect to time on February 24, 1997. As the visibility increased, we see a decrease in the number of dropouts.

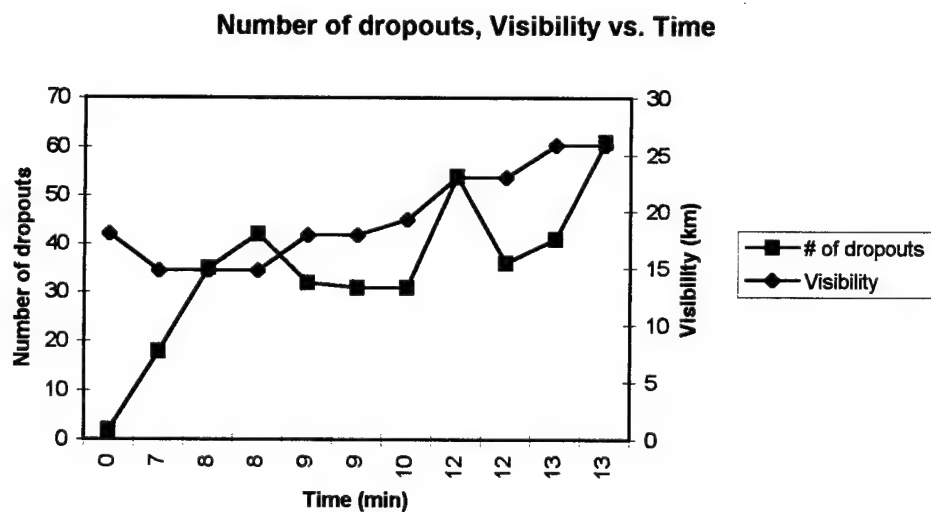


Figure 4.4 - Number of dropouts and visibility changing with respect to time on February 25, 1997. Surprisingly, as the visibility increases toward the end of the period, the number of dropouts does not change or increases.

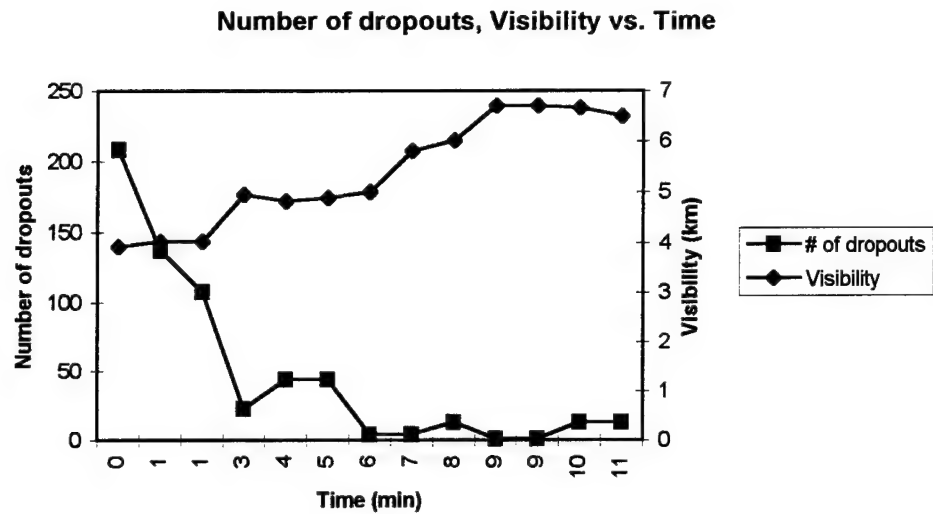


Figure 4.5 - Number of dropouts and visibility changing with respect to time on February 26, 1997. The number of dropouts gradually decreases with a slight improvement of visibility.

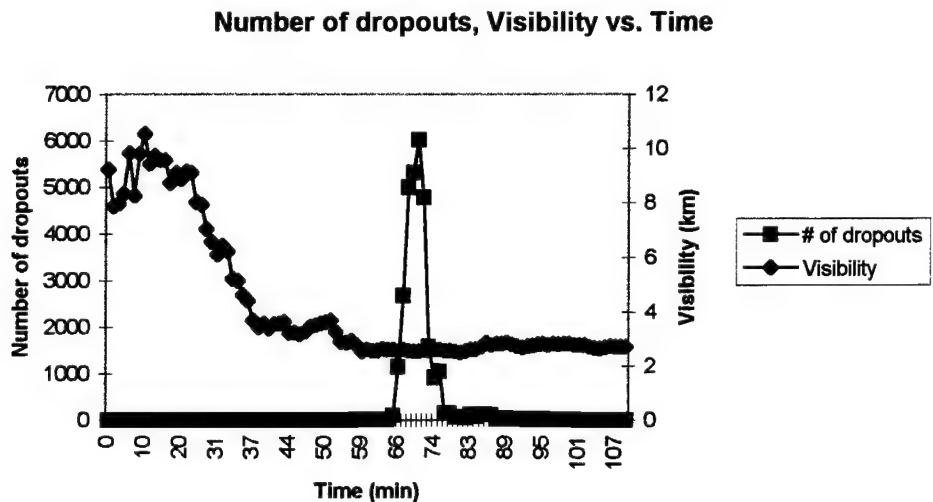


Figure 4.6 - Number of dropouts and visibility changing with respect to time on February 27, 1997. The number of dropouts stays fairly constant over the entire visibility range with the exception for one portion of the period.

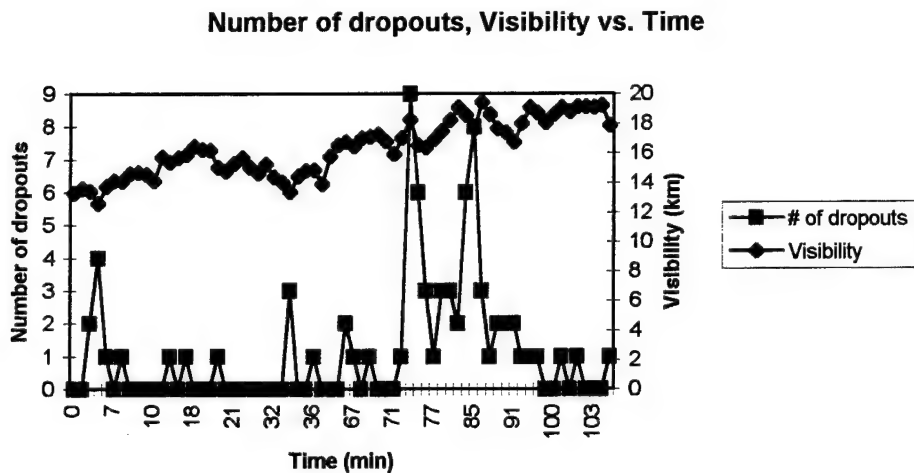


Figure 4.7 - Number of dropouts and visibility changing with respect to time on February 28, 1997. The visibility gradually increases while the number of dropouts remains fairly low.

4.2.2 - Dropouts and Rainfall Rate vs. Time

The following two graphs give an overall picture of the behavior of the dropouts with time, as well as an indication of how the rain rate was changing over that time.

Figures 4.8 and 4.9 represent February 24th and 25th, respectively.

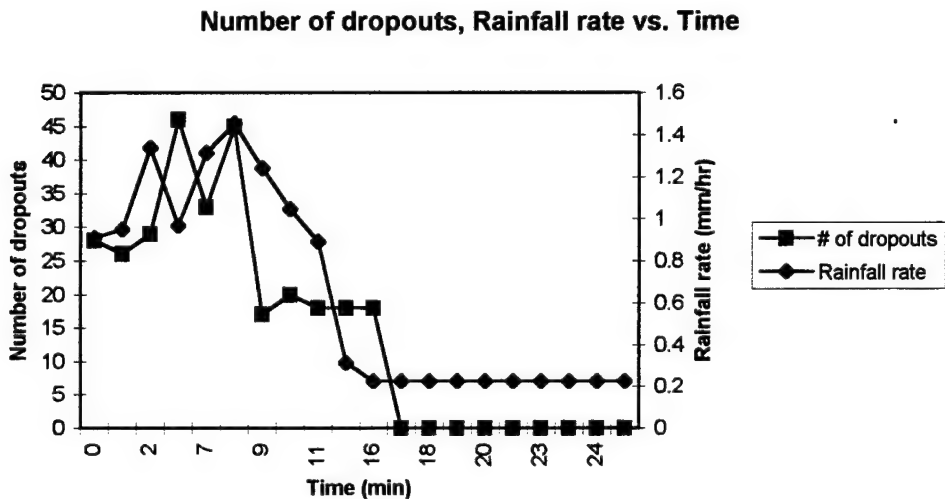


Figure 4.8 - Number of dropouts and rainfall rate changing with respect to time on February 24, 1997. As the rain tapers off, we see the number of dropouts fall to zero.

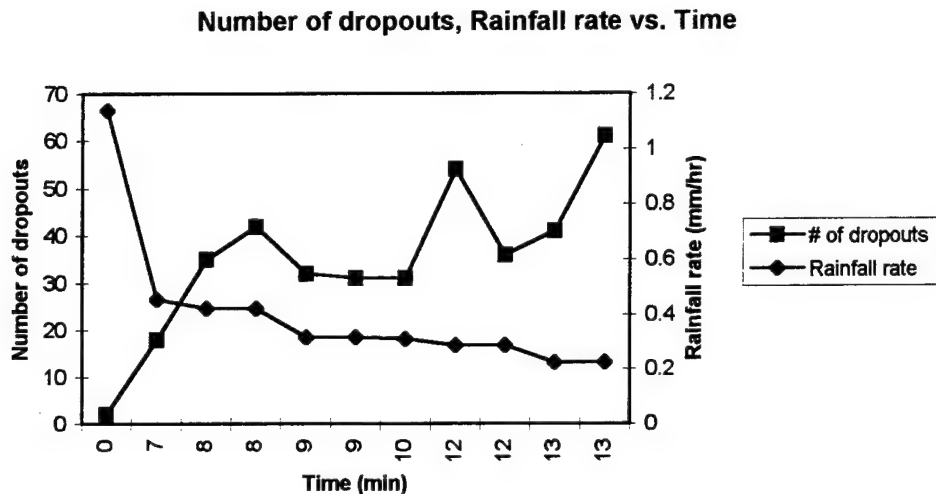


Figure 4.9 - Number of dropouts and rainfall rate changing with respect to time on February 25, 1997. Here we see very little change or an increase in the number of dropouts as the rain ends.

4.2.3 - False Returns and Visibility vs. Time

The following seven graphs give an overall picture of the behavior of the false returns with time, as well as an indication of how the visibility was changing over that time. Figures 4.10 - 4.16 represent January 3rd and February 19th, 24th, 25th, 26th, 27th, and 28th, respectively.

Number of false returns, Visibility vs. Time

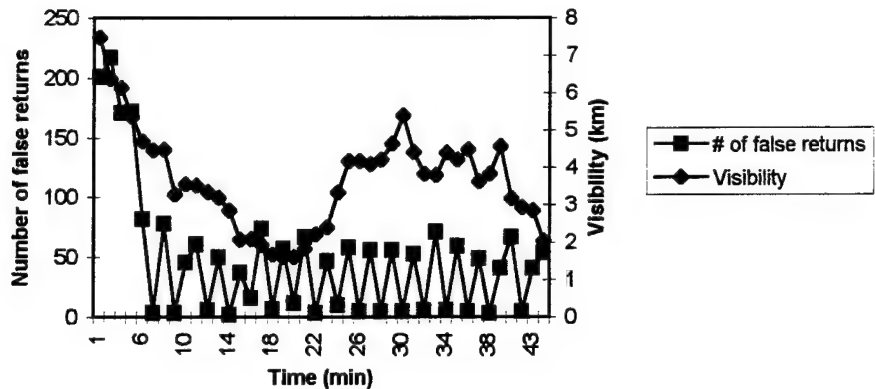


Figure 4.10 - Number of false returns and visibility changing with respect to time on January 3, 1997. The number of false returns fluctuates between ten and one hundred as the visibility decreases.

Number of false returns, Visibility vs. Time

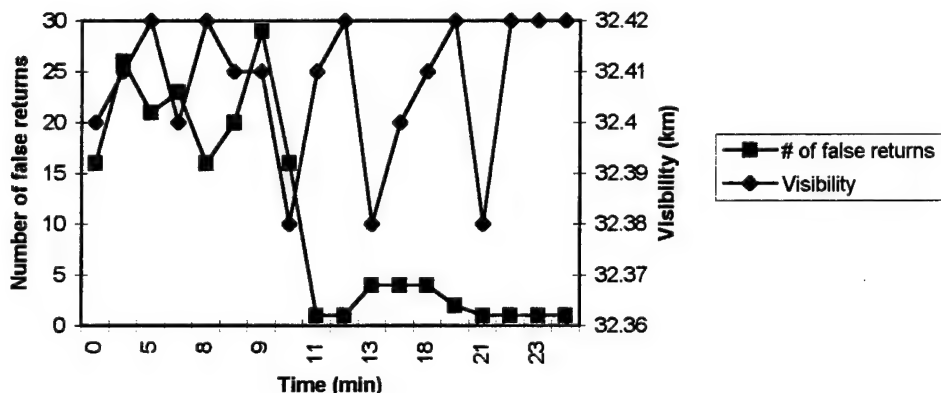


Figure 4.11 - Number of false returns and visibility changing with respect to time on February 19, 1997. False returns gradually taper off even though the visibility remains constant.

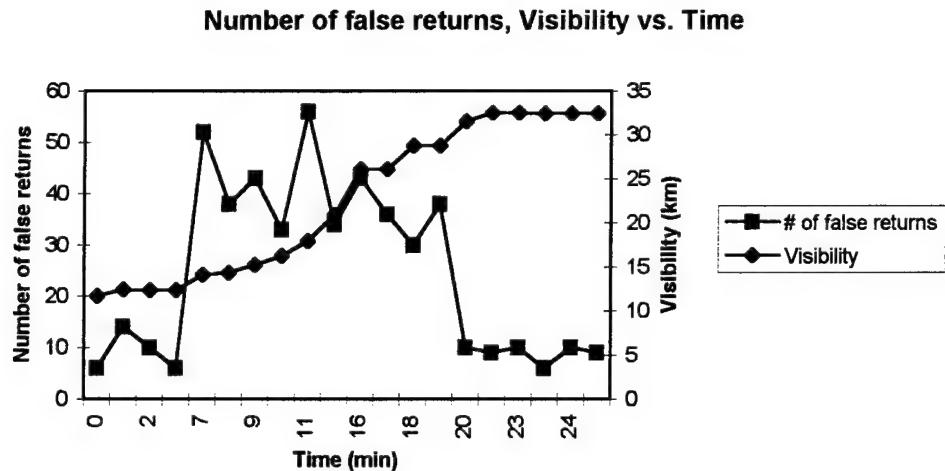


Figure 4.12 - Number of false returns and visibility changing with respect to time on February 24, 1997. Peak number is not paired with minimum visibility; however, as the visibility increases toward the end, the false return count decreases.

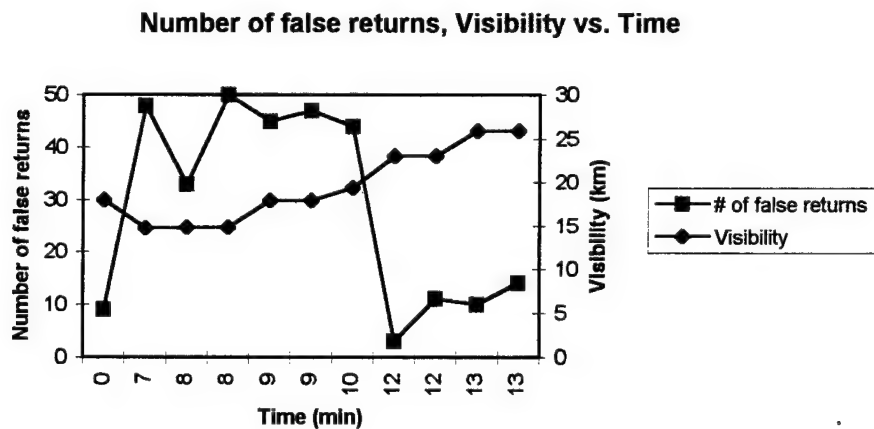


Figure 4.13 - Number of false returns and visibility changing with respect to time on February 25, 1997. False return count peaks at the minimum visibility and decreases as the visibility then increases.

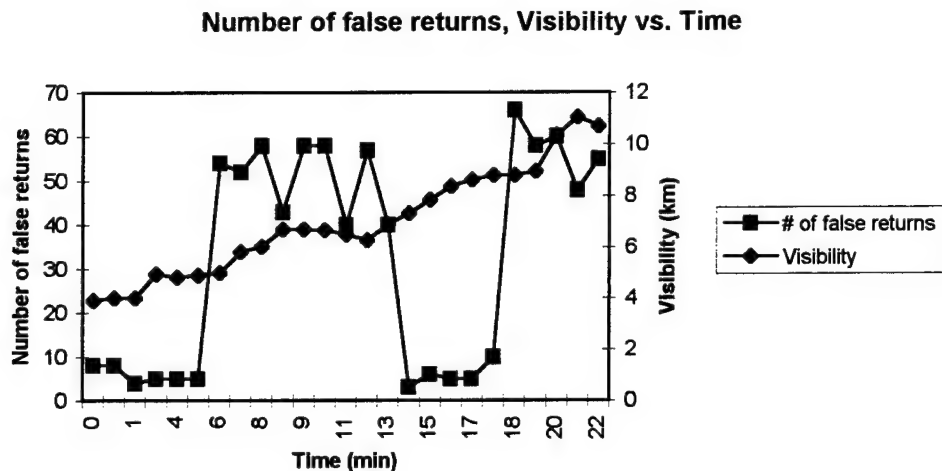


Figure 4.14 - Number of false returns and visibility changing with respect to time on February 26, 1997. The number of false returns hovers between zero and fifty, even though the visibility increases.

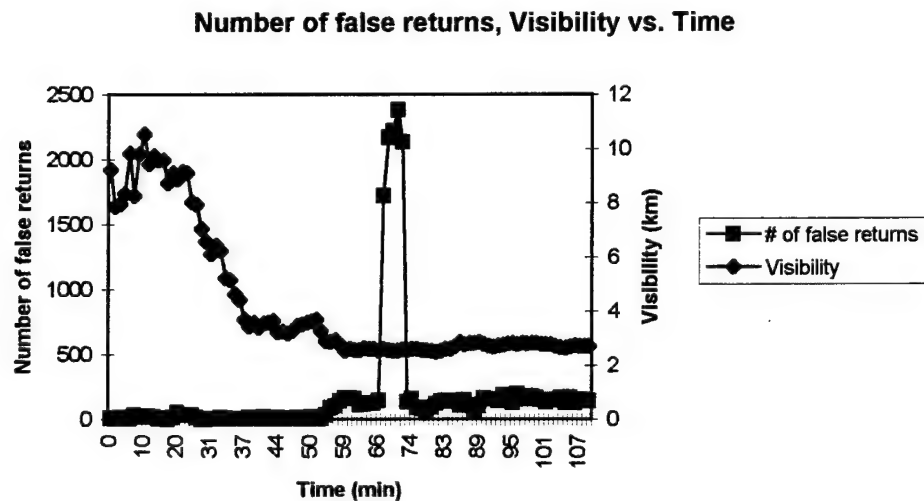


Figure 4.15 - Number of false returns and visibility changing with respect to time on February 27, 1997. The number of false returns remains fairly constant over the entire period with the exception of one portion of the period.

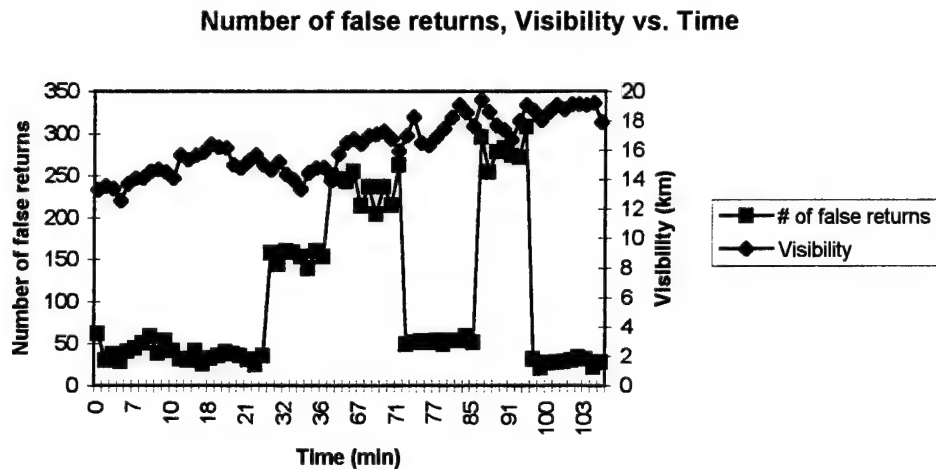


Figure 4.16 - Number of false returns and visibility changing with respect to time on February 28, 1997. As the visibility increases gradually, the number of false returns stays within the same order of magnitude.

4.2.4 - False Returns and Rainfall Rate vs. Time

The following two graphs give an overall picture of the behavior of the false returns with time, as well as an indication of how the rain rate was changing over that time. Figures 4.17 and 4.18 represent February 24th and 25th, respectively.

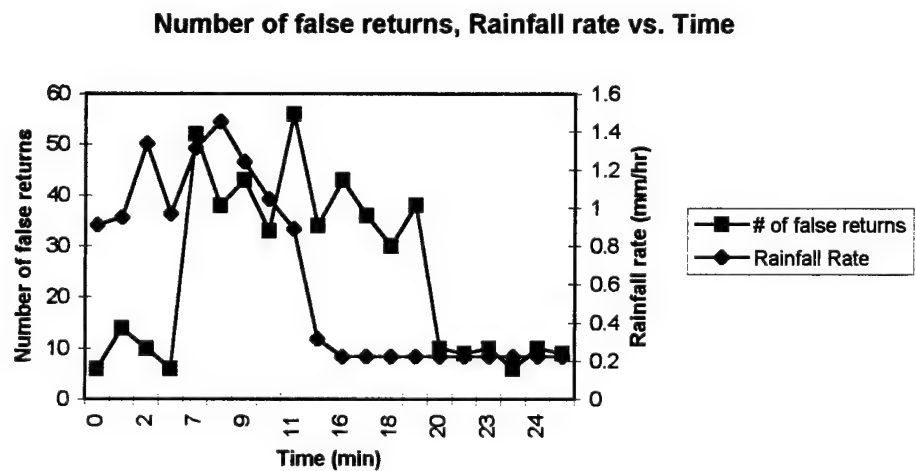


Figure 4.17 - Number of false returns and rainfall rate changing with respect to time on February 24, 1997. The number of false returns never gets very high, just like the rainfall rate.

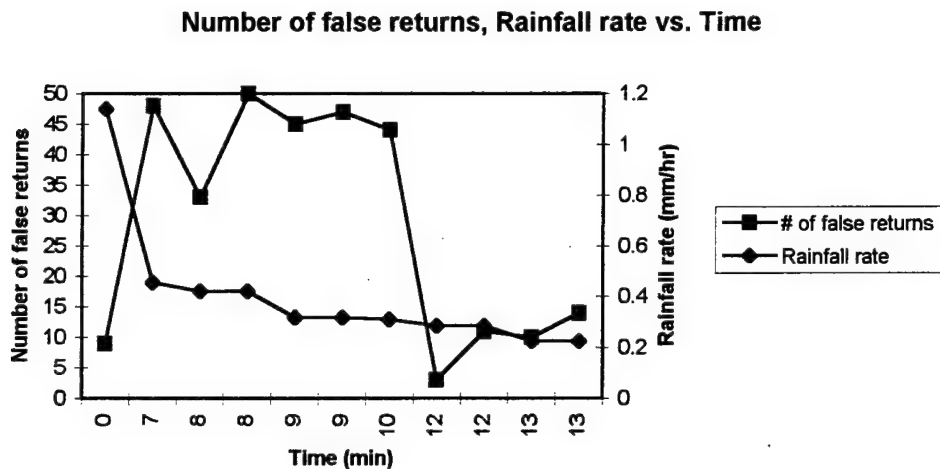


Figure 4.18 - Number of false returns and rainfall rate changing with respect to time on February 25, 1997. Here, we see a very low range of false return counts, as the rainfall rate gradually decreases.

4.2.5 - Dropouts vs. Visibility

For all dates, the number of dropouts showed a good response to changes in the weather. As the visibility decreased, the number would increase and vice versa. On some days, most of the points are clustered together, reflecting the small range of visibilities seen on that day.

Figure 4.19 shows the behavior of dropouts with visibility on January 3rd. There is some variability within the sample; however, most of the low visibilities have fairly high dropout counts, which is to be expected.

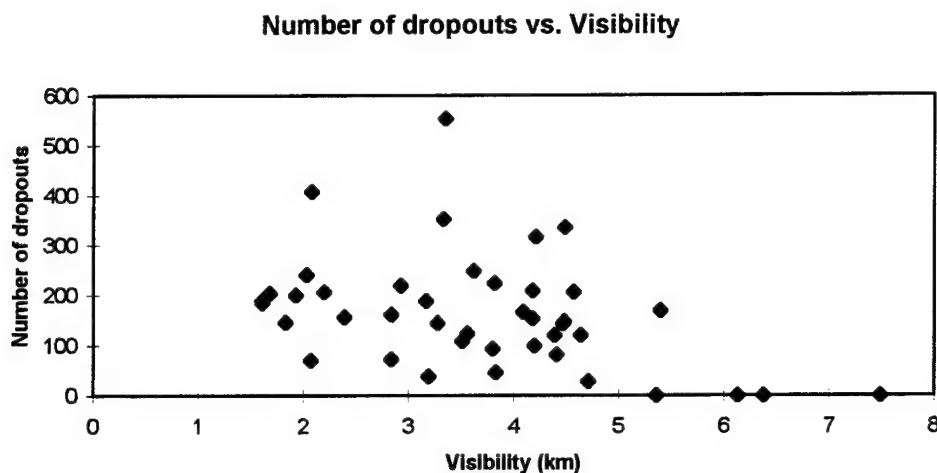


Figure 4.19 - Number of dropouts compared to visibility for January 3, 1997

Figure 4.20 shows the behavior of dropouts with visibility for February 19th. The visibility on this day was very good and did not vary greatly during the data collection period. The range of numbers for one visibility is very small, ± 10 returns.

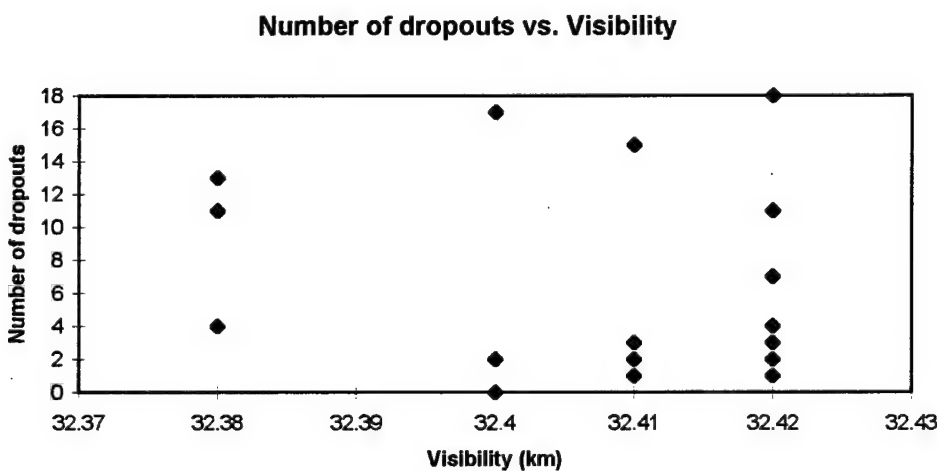


Figure 4.20 - Number of dropouts compared to visibility for February 19, 1997. Note the small visibility range on the x-axis.

Figure 4.21 shows the behavior of dropouts with visibility for February 24th. Here we see again that the number of dropouts is highest when the visibility is lowest.

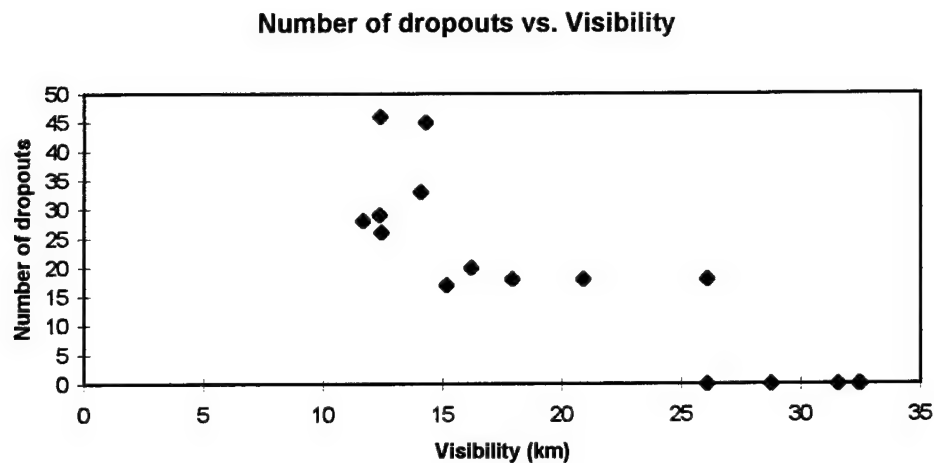


Figure 4.21 - Number of dropouts compared to visibility for February 24, 1997

Figure 4.22 shows the behavior of dropouts with visibility for February 25th while Figure 4.23 shows the behavior on February 26th. Figure 4.22 shows that the highest numbers were with the highest visibilities. But on this day, the visibility remained fairly constant, and the range of dropouts was fairly small. In Figure 4.23, the number of dropouts tends to increase with decreasing visibility.

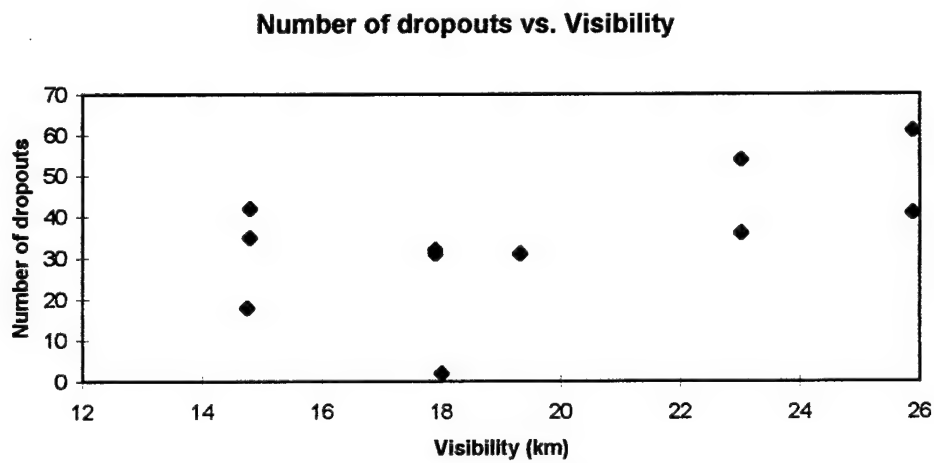


Figure 4.22 - Number of dropouts compared to visibility for February 25, 1997

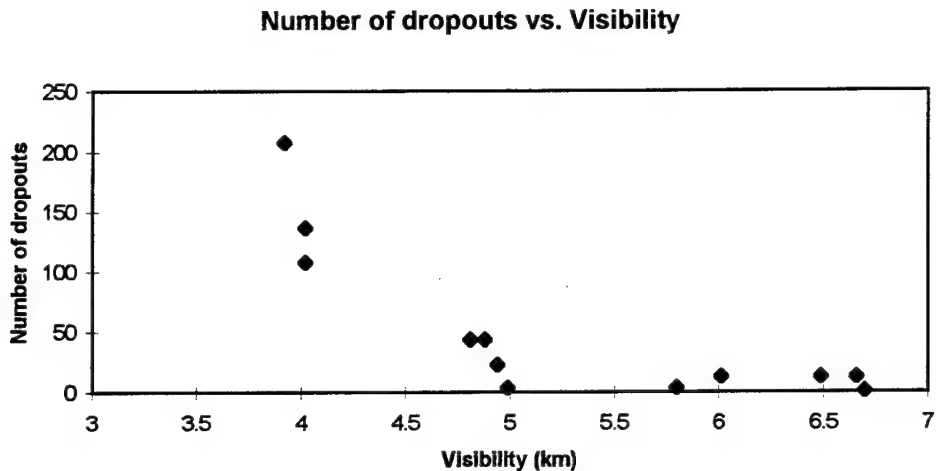


Figure 4.23 - Number of dropouts compared to visibility for February 26, 1997

Figure 4.24 shows the behavior of dropouts with visibility for February 27th. We see a gradual decrease in the number of dropouts as the visibility increases. Plus, there is a large range of dropout counts for near the minimum visibility value.

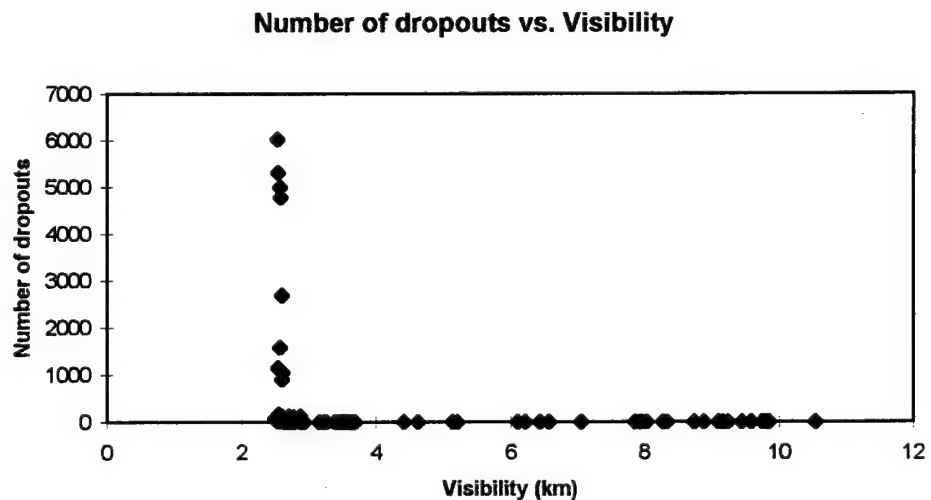


Figure 4.24 - Number of dropouts compared to visibility for February 27, 1997

Figure 4.25 shows the behavior of dropouts with visibility for February 28th, the final day. On this day, the number of dropouts remained fairly constant over all visibilities.

There are a few apparent outliers, but they are only slightly larger than the majority of the readings.

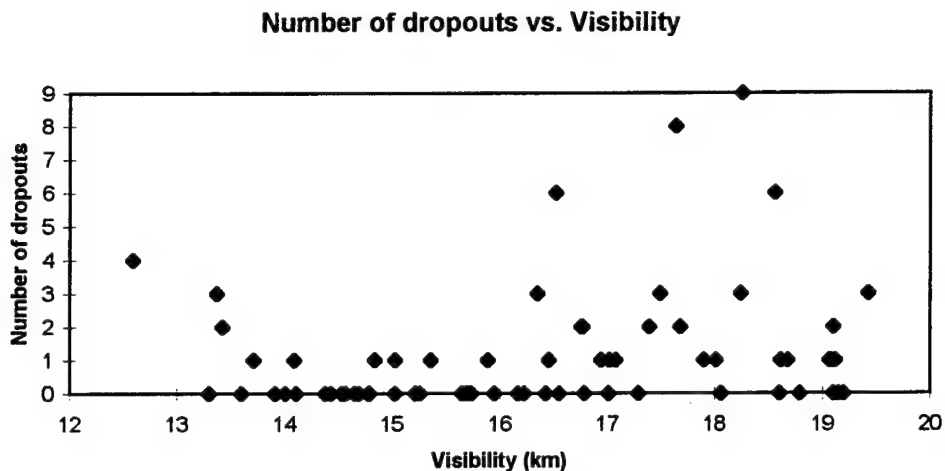


Figure 4.25 - Number of dropouts compared to visibility for February 28, 1997

Figure 4.26 is a composite graph of number of dropouts versus visibility over all days. We can see that as visibility decreased the number of returns did increase, and that the pattern of points indicates that a non-linear relationship exists between the two variables.

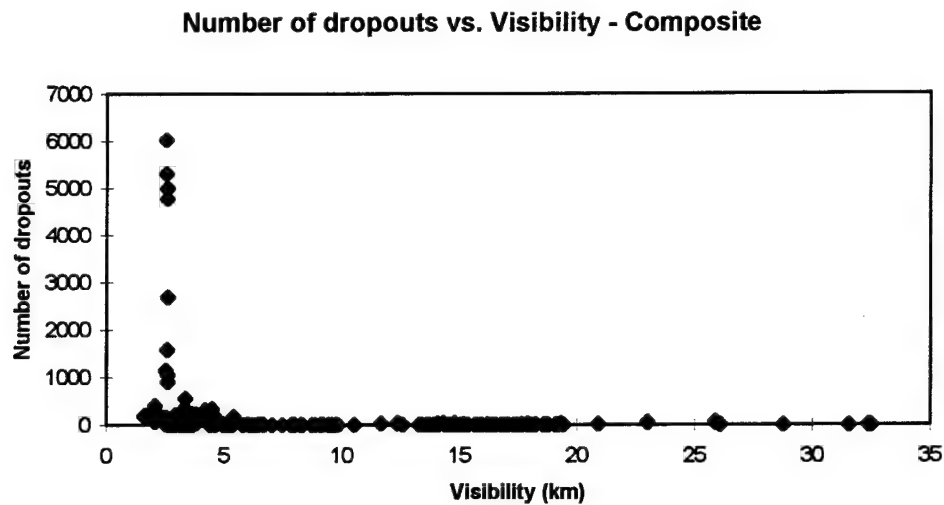


Figure 4.26 - Composite graph of number of dropouts vs. visibility. Note the highly non-linear shape of the grouping of points.

4.2.6 - Dropouts vs. Rain Rate

Rain only fell on two of the days, February 24th and February 25th. Figure 4.27 shows the number of dropouts versus rainfall rate for the 24th, and Figure 4.28 shows the number of dropouts versus rainfall rate for the 25th. Figure 4.27 indicates that as the rainfall rate increased, the number of dropouts remains fairly constant or increases slightly. Figure 4.28 shows a little different picture, with the highest number with the lowest rainfall rates.

Number of dropouts vs. Rainfall rate

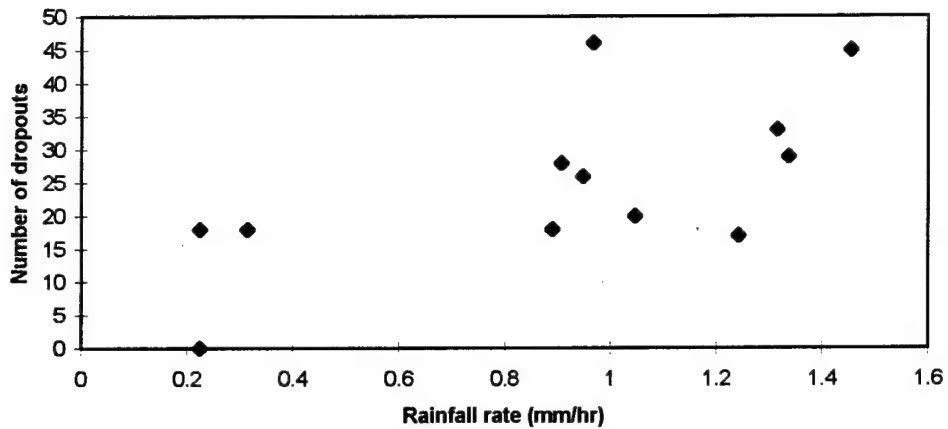


Figure 4.27 - Number of dropouts compared to rainfall rate for February 24, 1997

Number of dropouts vs. Rainfall rate

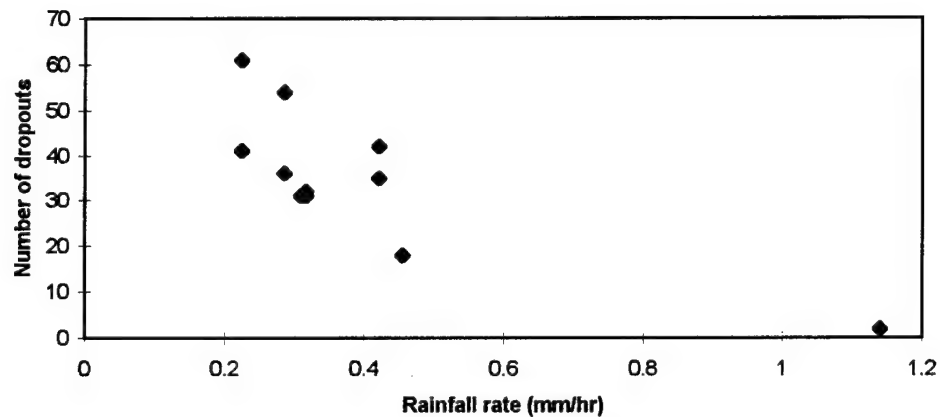


Figure 4.28 - Number of dropouts compared to rainfall rate for February 25, 1997

Figure 4.29 is a composite graph of number of dropouts versus rainfall rate over all days. The number of returns remains fairly constant as the rainfall rate changes, so dropouts are not as sensitive to rainfall.

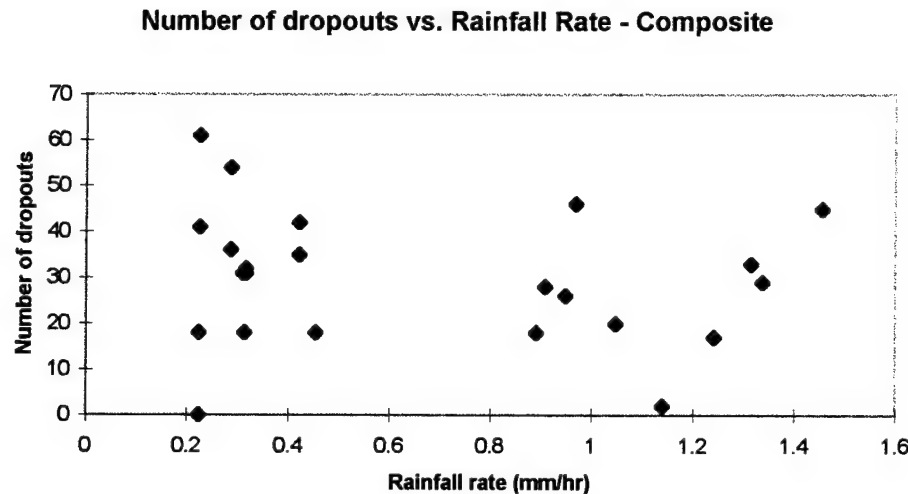


Figure 4.29 - Composite graph of number of dropouts vs. rainfall rate.

4.2.7 - False Returns vs. Visibility

The behavior of the number of false returns with respect to visibility is not as predictable as the dropouts. The behavior exhibited is not necessarily what would be expected with the changing weather conditions.

Figure 4.30 exhibits number of false returns and visibility for January 3rd. The highest number of returns is found with the highest visibility, not what would be expected. But overall, most of the points are clustered between zero and 100.

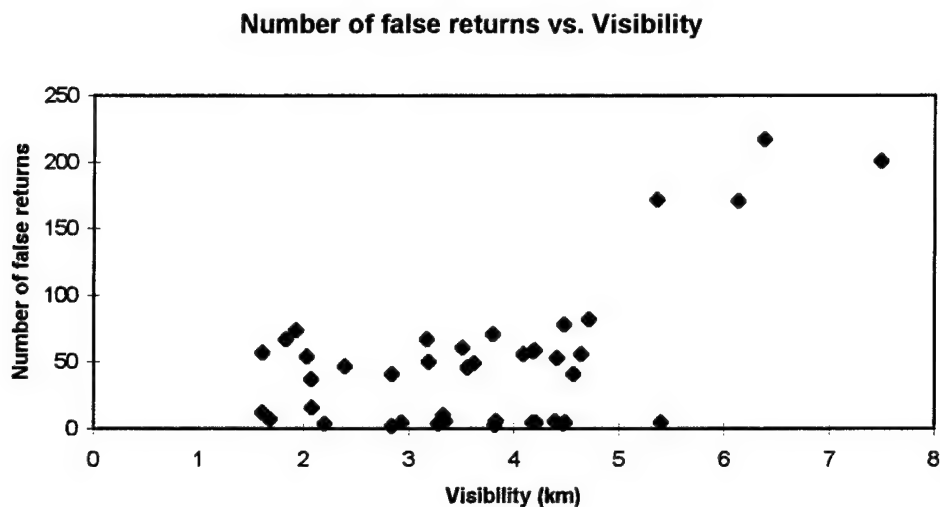


Figure 4.30 - Number of false returns compared to visibility for January 3, 1997

Figure 4.31 exhibits number of false returns and visibility for February 19th. We see a range of returns at one visibility (due to the limited range of visibilities on this day); however, the range is very small.

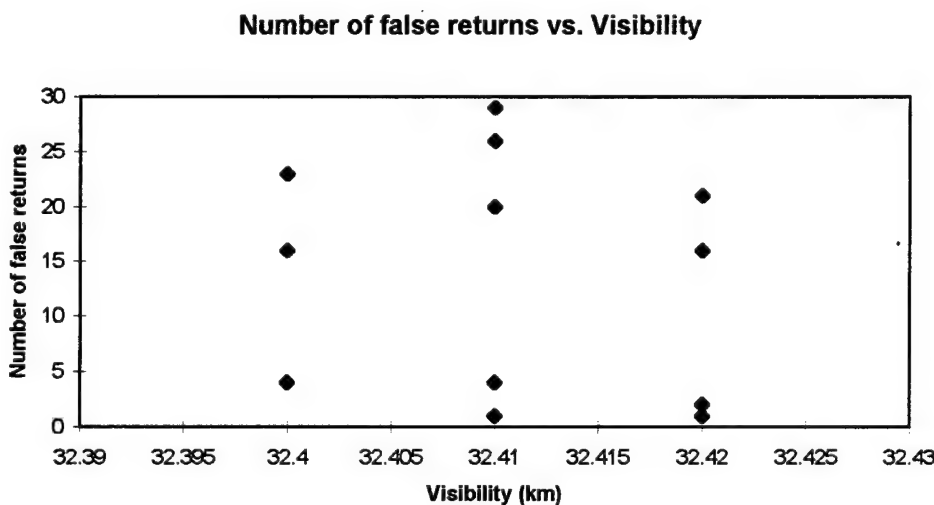


Figure 4.31 - Number of false returns compared to visibility for February 19, 1997

Figure 4.32 exhibits number of false returns and visibility for February 24th, and Figure 4.33 exhibits number of false returns and visibility for February 25th. Figure 4.32 shows groups of low counts at the highest and lowest visibilities, with the highest values

found in the middle visibility range. Figure 4.33 shows a more expected relationship where the highest counts are with the lowest visibilities and vice versa.

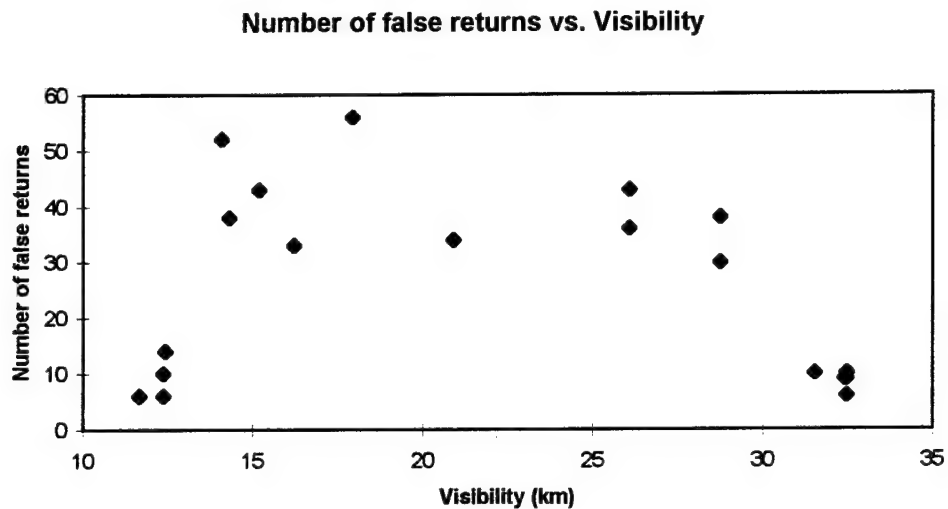


Figure 4.32 - Number of false returns compared to visibility for February 24, 1997

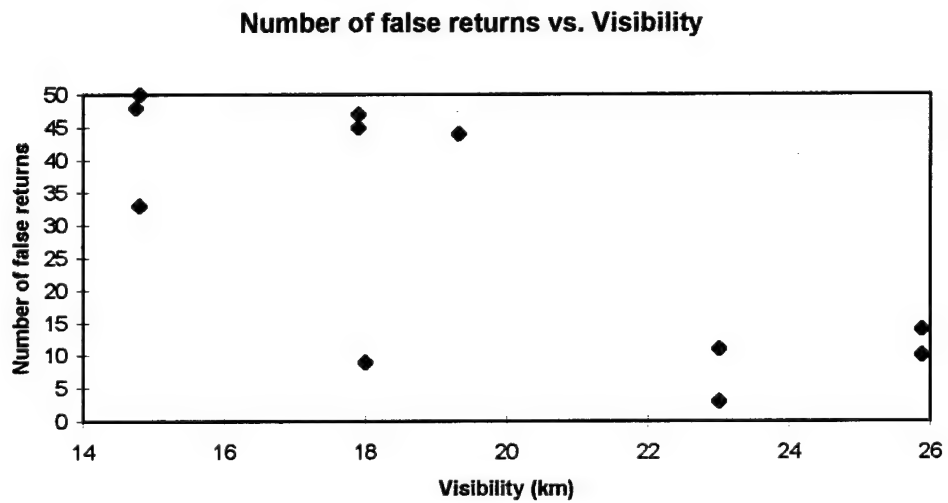


Figure 4.33 - Number of false returns compared to visibility for February 25, 1997

Figure 4.34 exhibits number of false returns and visibility for February 26th, and Figure 4.35 shows the number of false returns and visibility for February 27th. In Figure 4.34, the highest counts are with a mid and a high value of visibility while the higher counts are clustered at the lowest and a mid value of visibility. Figure 4.35 shows that the

number of false returns decreases with increasing visibility, and the maximum number of false returns is clustered near the minimum visibility.

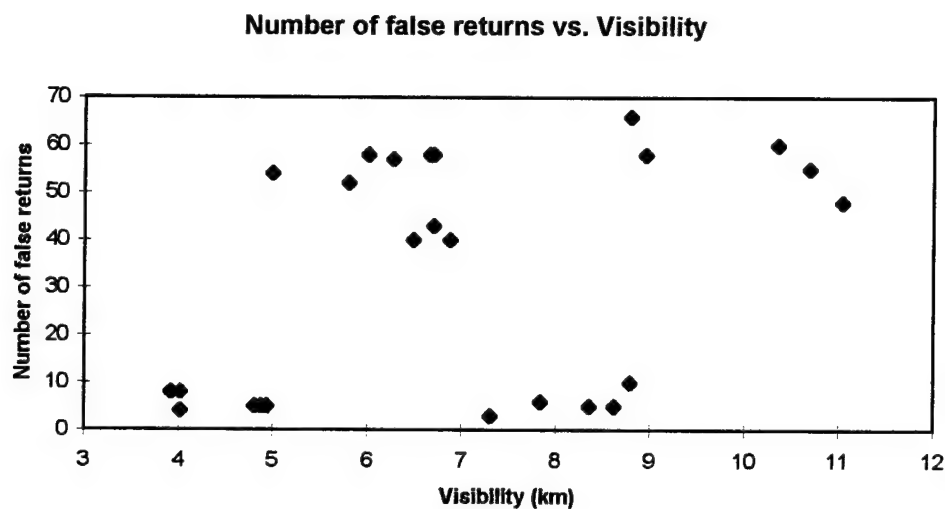


Figure 4.34 - Number of false returns compared to visibility for February 26, 1997

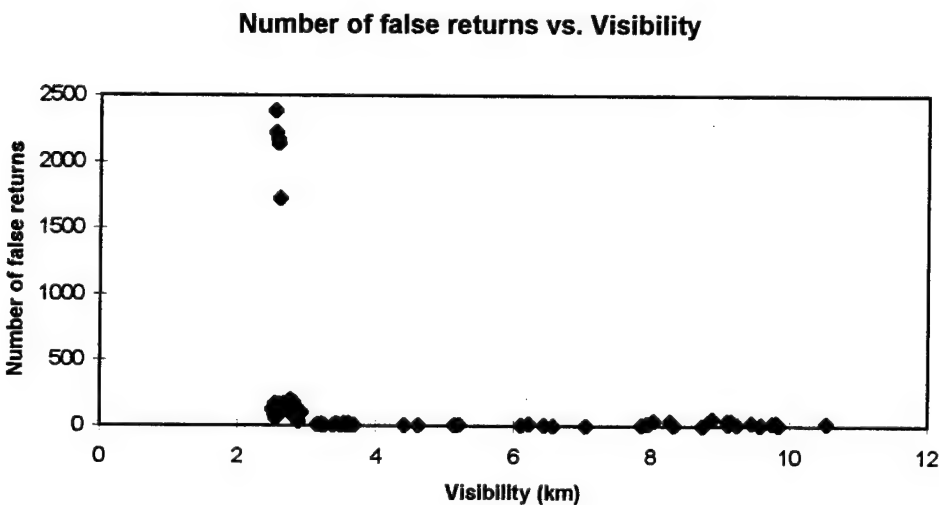


Figure 4.35 - Number of false returns compared to visibility for February 27, 1997

Figure 4.36 exhibits number of false returns and visibility for February 28th. It shows that most of the counts are clustered near zero with other higher points scattered throughout the range of visibilities.

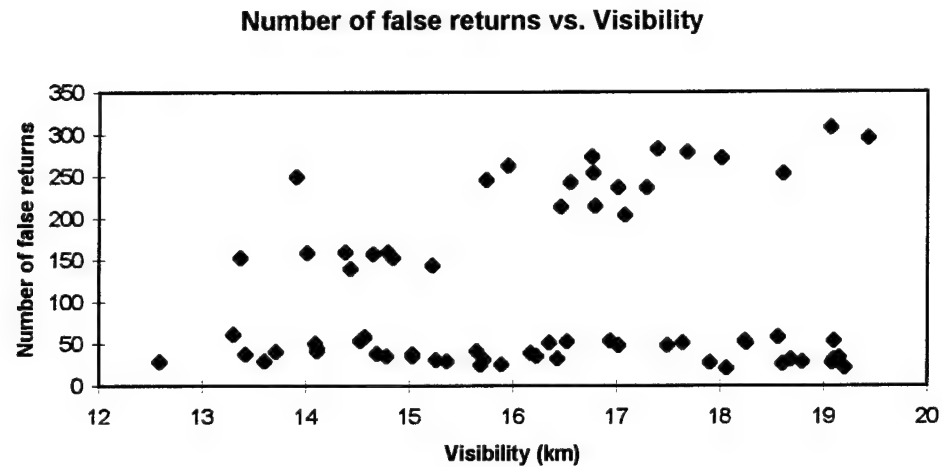


Figure 4.36 - Number of false returns compared to visibility for February 28, 1997

Figure 4.37 is a composite graph of number of false returns versus visibility over all days. We can see that the number of false returns remains fairly constant over the entire range of visibilities, except for three groups near six, fifteen, and eighteen kilometers.

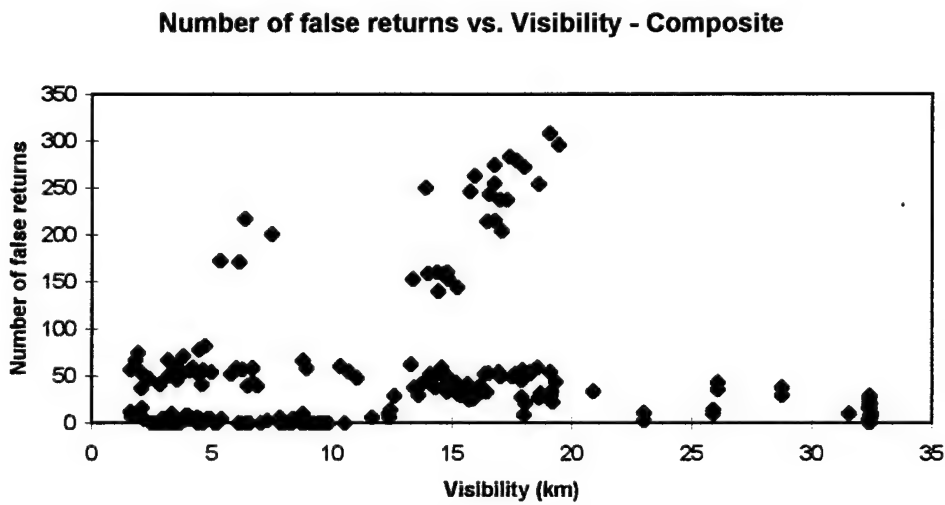


Figure 4.37 - Composite graph of number of false returns vs. visibility

4.2.8 - False Returns vs. Rainfall Rate

Figure 4.38 shows the number of false returns versus rainfall rate for February 24th, and Figure 4.39 shows the number of false returns versus rainfall rate for February 25th. Once again, the number of false returns does not act as expected with rain rate. The higher rain rates do not necessarily show higher numbers of false returns. Plus, there is some variability for one individual rain rate.

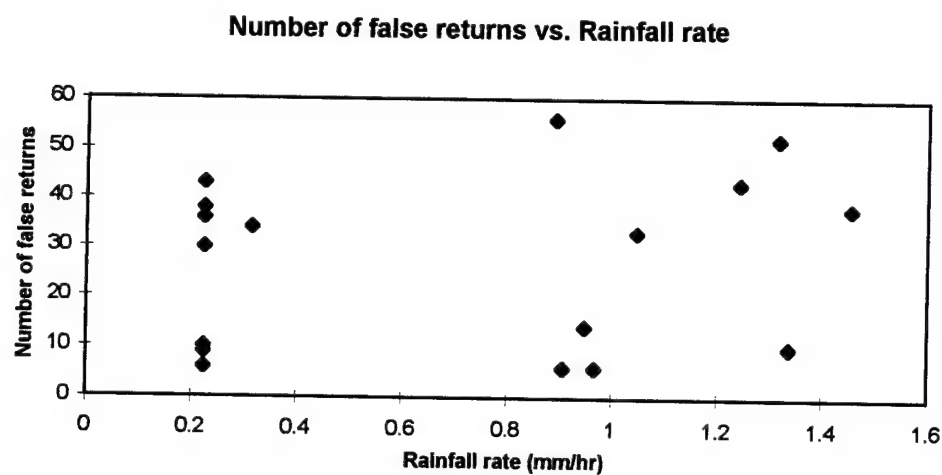


Figure 4.38 - Number of false returns compared to rainfall rate on February 24, 1997

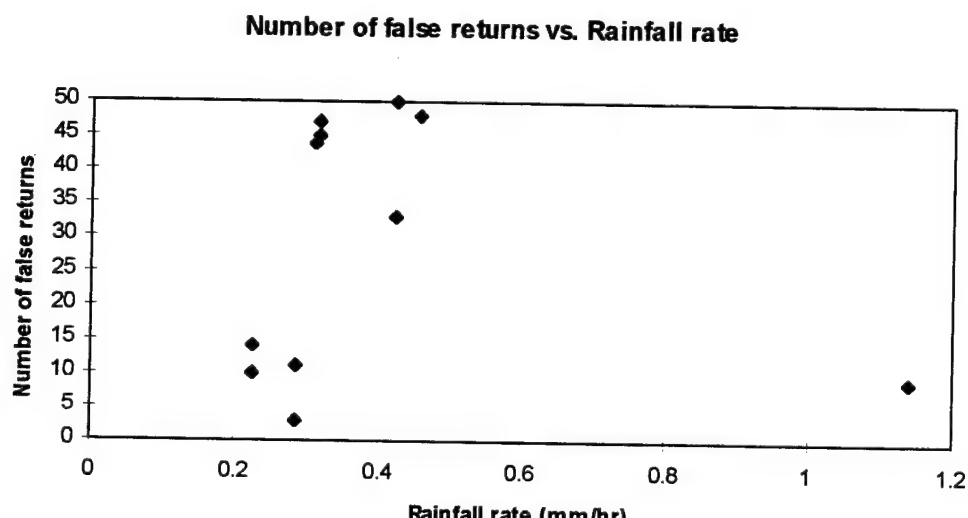


Figure 4.40 is a composite graph of number of false returns versus rainfall rate over all days. The data points are very scattered and show no real pattern—demonstrating how changes in the number of false returns were not as predictable as changes in the number of dropouts.

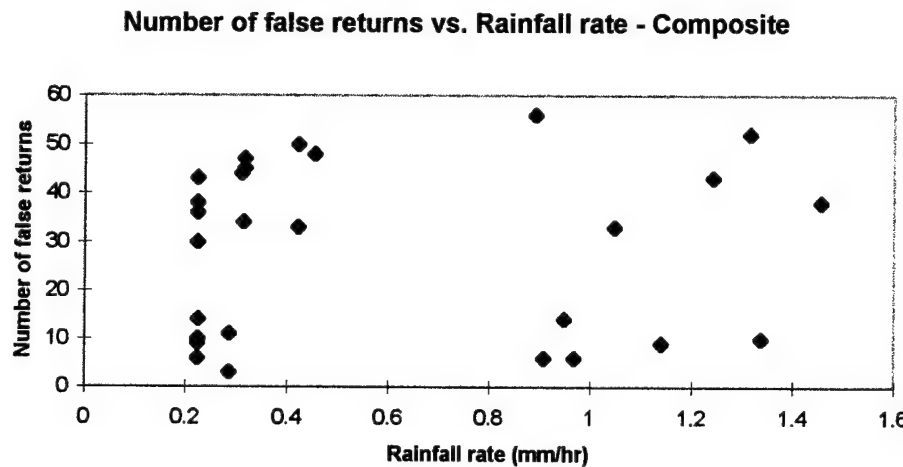


Figure 4.40 - Composite graph of number of false returns vs. rainfall rate

4.2.9 - Extinction and Dropouts vs. Time

Over time on any particular day, the visibility was changing, so extinction should also be changing since the two variables are related according to Koschmeider's Law. Changes in extinction are helpful in seeing how the degradation of the laser beam is changing over time.

Figures 4.41 - 4.47 show the variation of extinction over time, with the number of dropouts, for the six dates of concern here, January 3rd and February 19th, 24th, 25th, 26th, 27th, and 28th. The number of dropouts are included to see how changes in dropouts were reflected in changes in extinction.

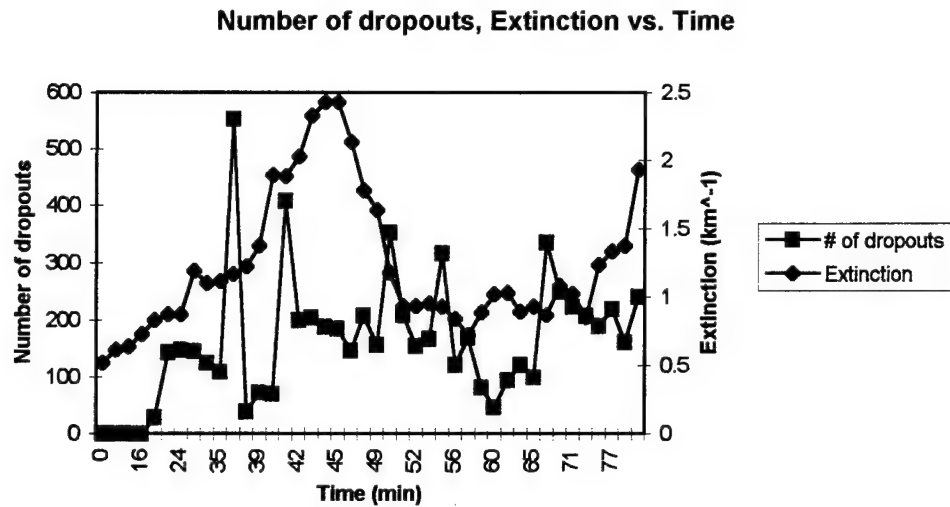


Figure 4.41 - Extinction coefficient β as it varied over time on January 3, 1997. Extinction is represented by a solid line, and dropouts are represented by a dashed line. You can see an increase in the number of dropouts as β reaches a peak.

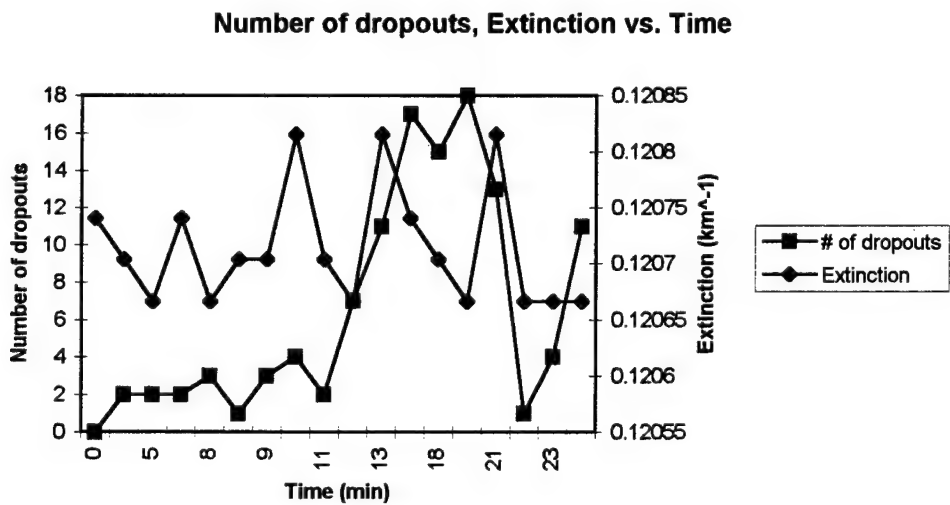


Figure 4.42 - Extinction coefficient β as it varied over time on February 19, 1997. Since β changes very little, the number of dropouts does not react very much to the change.

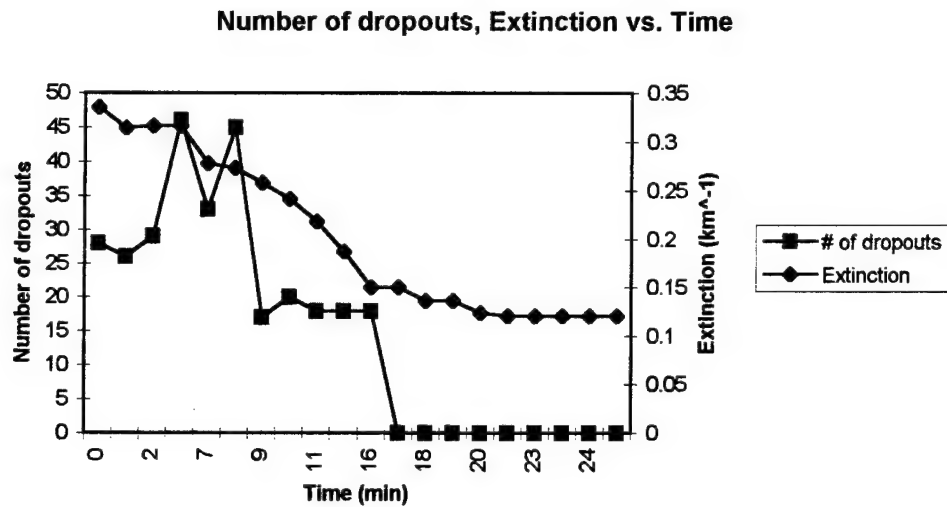


Figure 4.43 - Extinction coefficient β as it varied over time on February 24, 1997. Here we see that as extinction decreases, the number of dropouts also decreases.

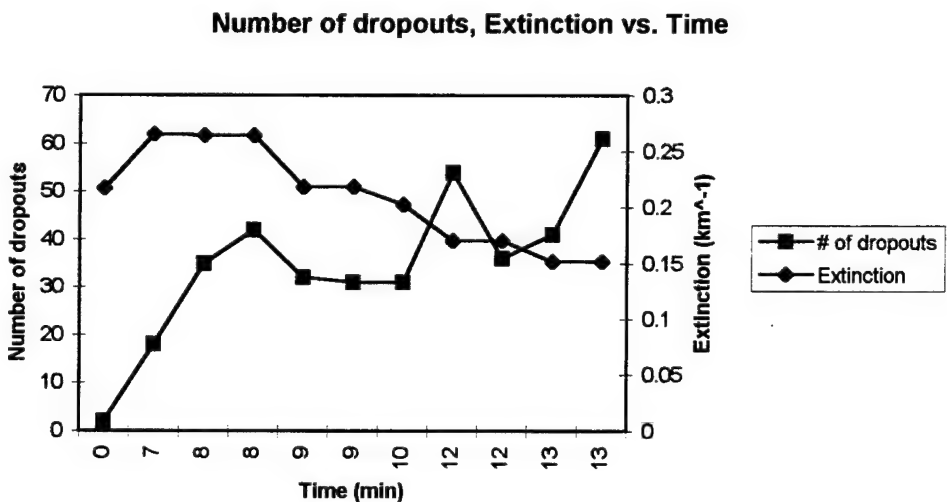


Figure 4.44 - Extinction coefficient β as it varied over time on February 25, 1997. Here the peak extinction is very close to a peak in dropouts; however, the dropouts do continue to increase slightly as the extinction decreases.

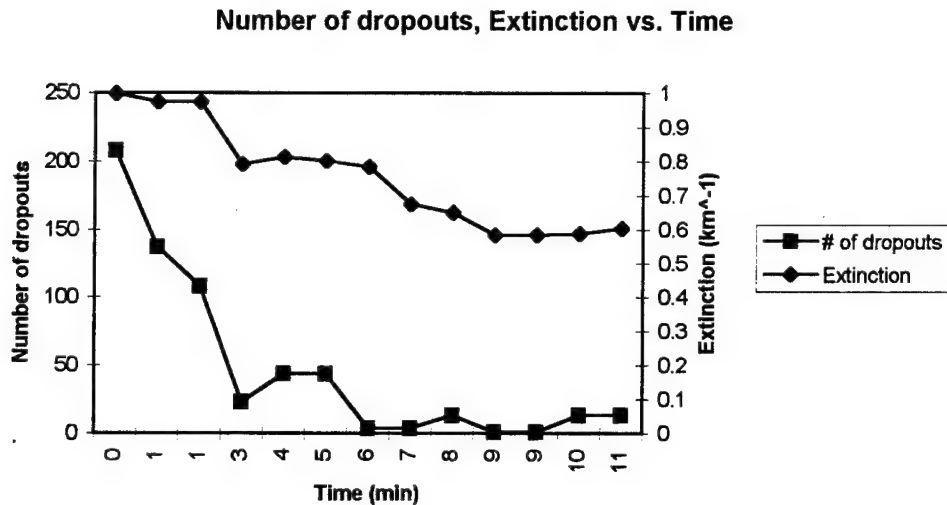


Figure 4.45 - Extinction coefficient β as it varied over time on February 26, 1997. We see very little change in dropouts as extinction decreases. The largest change in dropouts is found at the beginning of the period.

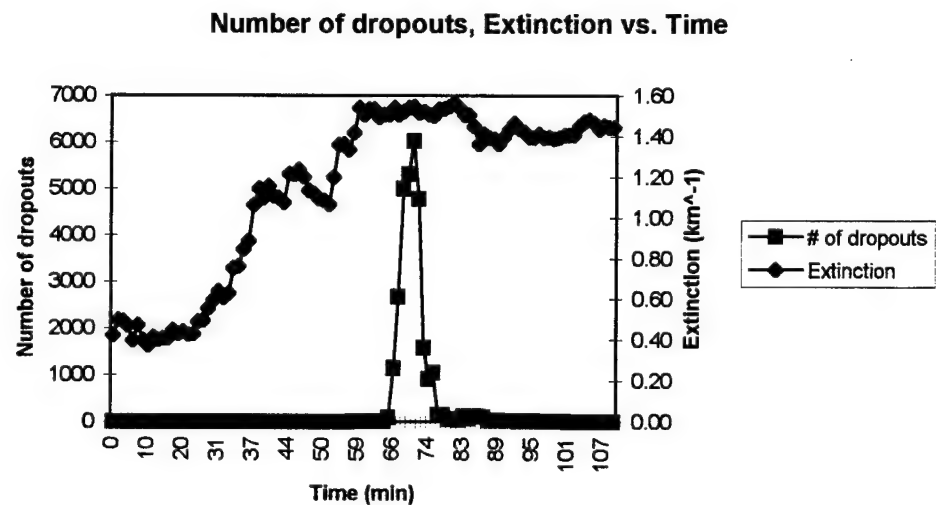


Figure 4.46 - Extinction coefficient β as it varied over time on February 27, 1997. We see the peak in extinction (minimum in visibility) is paired with a large peak in the number of dropouts

Number of dropouts, Extinction vs. Time

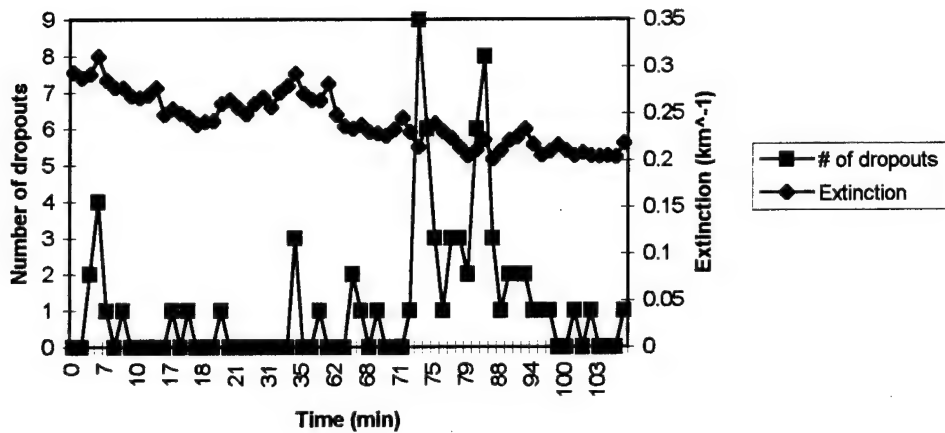


Figure 4.47 - Extinction coefficient β as it varied over time on February 28, 1997. Extinction changes very little over time, and the number of dropouts changes very little as well.

Figure 4.48 is a composite graph of number of dropouts versus extinction coefficient over all days. We can see when the extinction is low (high visibility) the number of dropouts is also low, a result we would expect. Plus we see an increase in the number of dropouts as the extinction increases (visibility decreases). The scale on the y-axis is reduced due to the large number of dropouts recorded on February 27th. This allows the lower portion of the graph to stand out better.

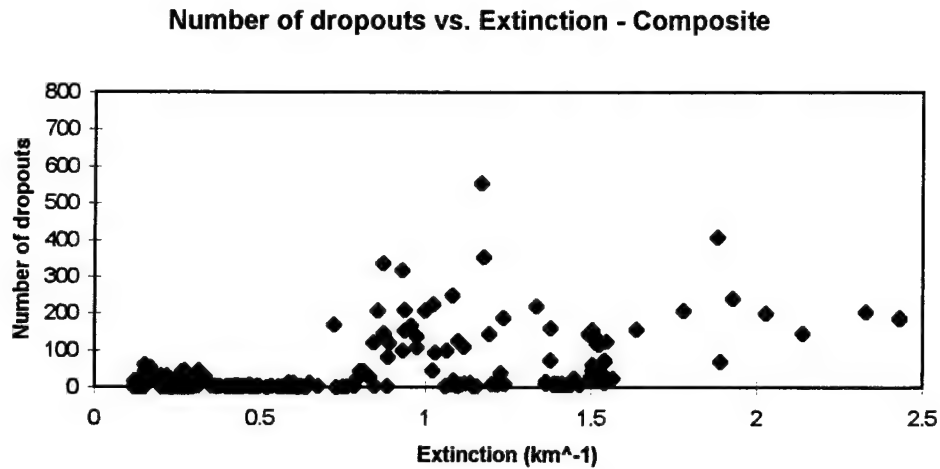


Figure 4.48 - Composite graph of number of dropouts vs. extinction coefficient

4.3 - Control Charts for Various Variables

Control charts were constructed to study the behavior of the dropouts and false returns. Since the ladar system operated consistently, the weather was the only variable between images; therefore, the impact of the changes in the weather could be assessed by a control chart. The charts were also used to show that the weather influence was indeed a significant influence in the behavior of the system. Control charts for number of dropouts, number of false returns, visibility, and rain rate identify the lack of control and strong influence of the weather on the ladar system.

Note: Lower control limits less than zero are assigned the value of zero.

4.3.1 - January 3, 1997

The control charts for number of dropouts, number of false returns, and visibility for January 3rd are pictured below, Figures 4.49-4.51. Figure 4.49, control chart for dropouts, shows two outlier dropouts which fall above the upper control limit and many runs of various length, mostly above the mean.

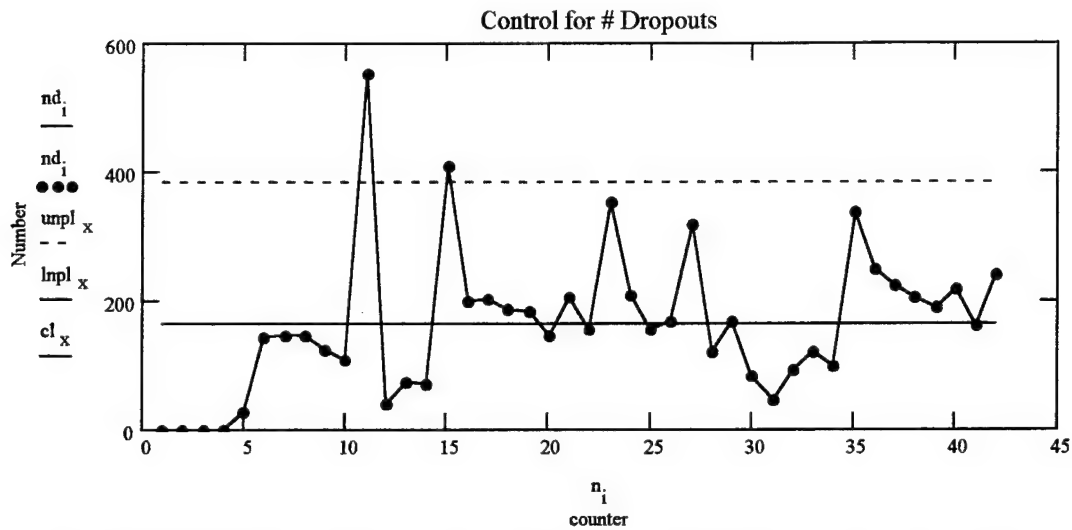


Figure 4.49 - Statistical control chart for number of dropouts over time for January 3, 1997

Figure 4.50, control chart for false returns, shows a fairly well behaved set of data, as the false returns hover around the mean, except for the beginning of the data set. However, the upper control limit is very high with respect to the rest of the values in the data set, so it may be biased and skew the chart.

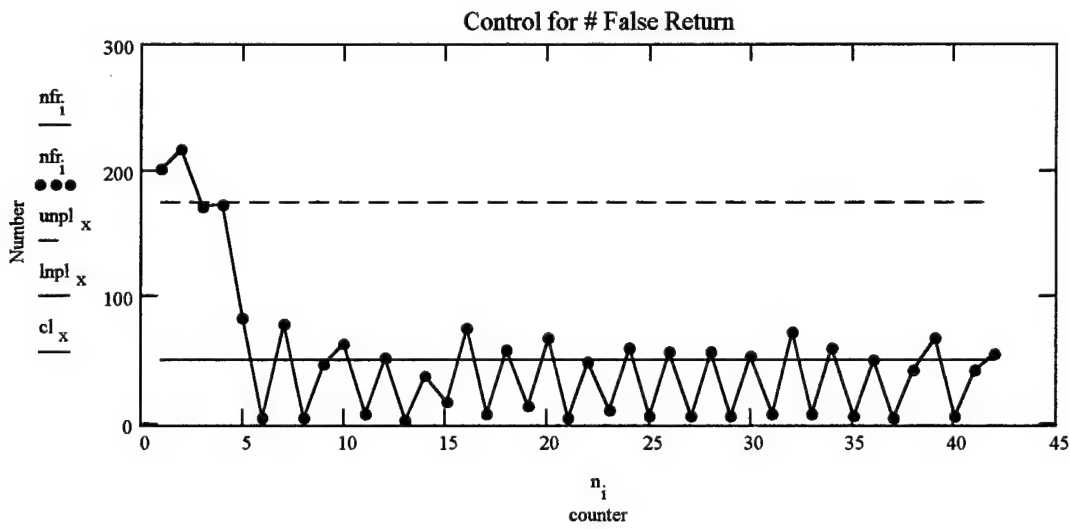


Figure 4.50 - Statistical control chart for number of false returns over time for January 3, 1997

Figure 4.51 shows the behavior of the visibility for the 3rd. It clearly shows that the visibility is not a random influence on the system. The visibility is constantly increasing or decreasing, not changing due to something which the operator of the system can control.

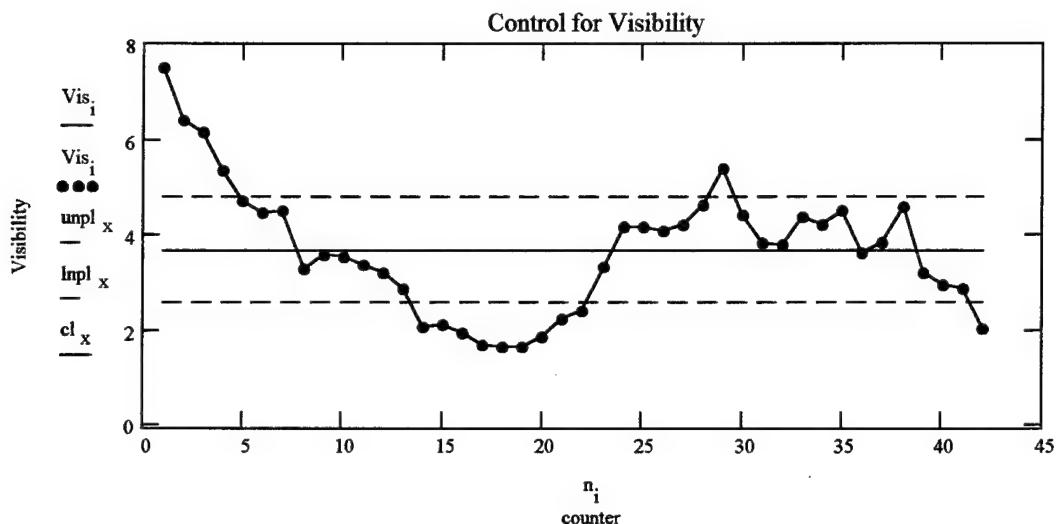


Figure 4.51 - Statistical control chart for visibility over time for January 3, 1997

4.3.2 - February 19, 1997

The control charts for number of dropouts, number of false returns, and visibility for February 19th are pictured below, Figures 4.52-4.54. Figure 4.52, control chart for dropouts, shows that the values for number of dropouts never center on the mean and are very erratic in their behavior.

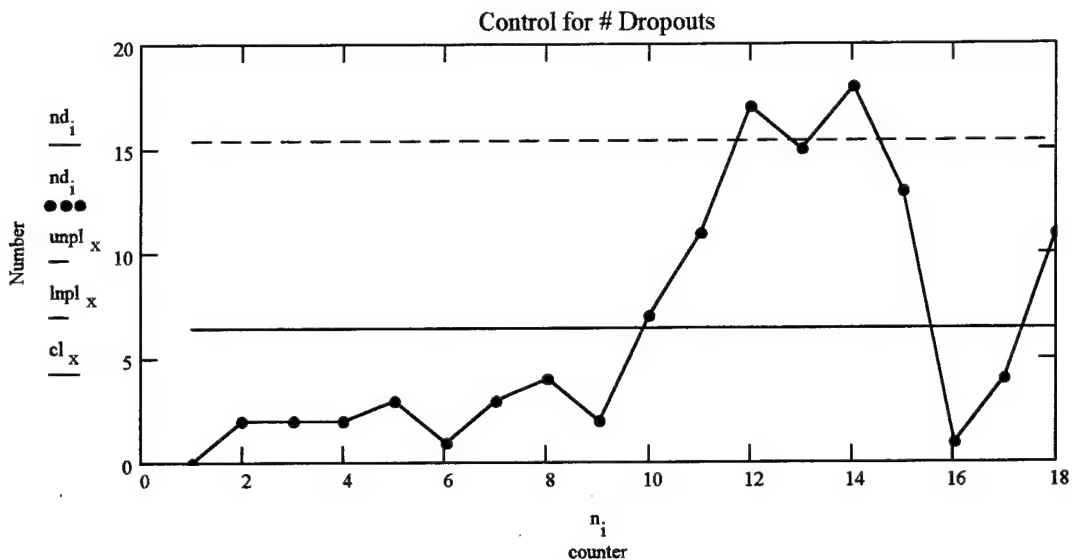


Figure 4.52 - Statistical control chart for number of dropouts over time on February 19, 1997

Figure 4.53, control chart for false returns, shows a pattern similar to that for the number of dropouts. The false return values are not centered and are very erratic in placement.

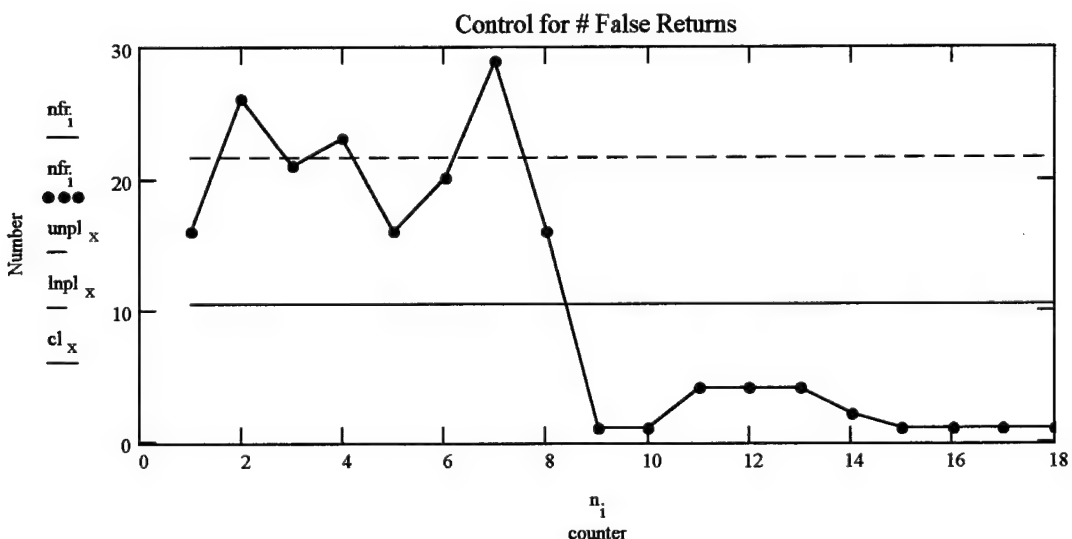


Figure 4.53 - Statistical control chart for number of false returns over time on February 19, 1997

Figure 4.54, control chart for visibility, reflects the fact that the visibility was fairly constant on this day. The values are centered around the mean, and there are no significant runs or outliers.

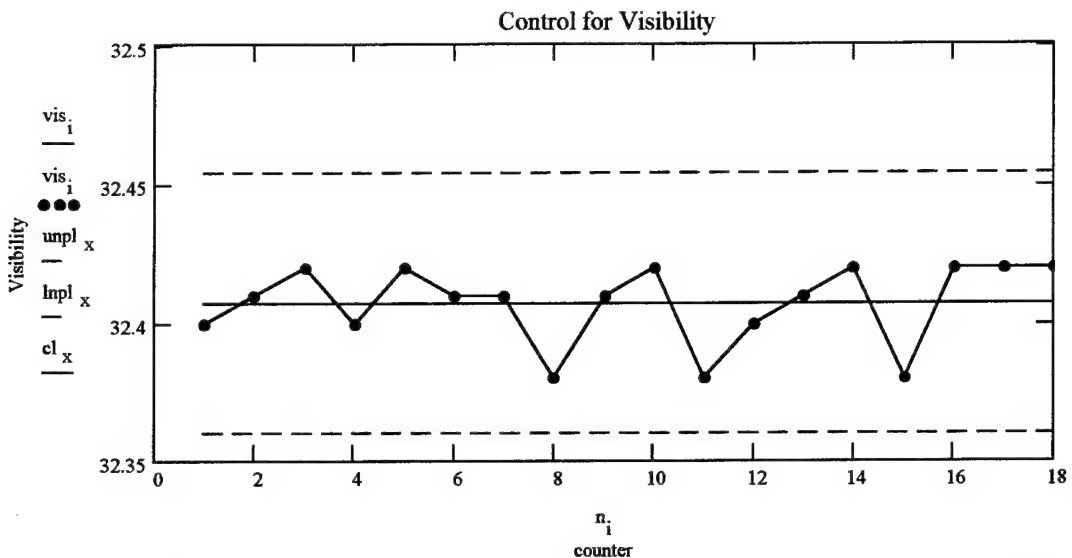


Figure 4.54 - Statistical control chart for visibility over time on February 19, 1997

4.3.3 - February 24, 1997

The control charts for number of dropouts, number of false returns, rain rate, and visibility for February 24th are pictured below, Figures 4.55-4.58. In Figure 4.55, the control chart for dropouts shows that the process is very much out of control. The values for dropouts are not centered, are erratic, and have runs both above and below the mean.

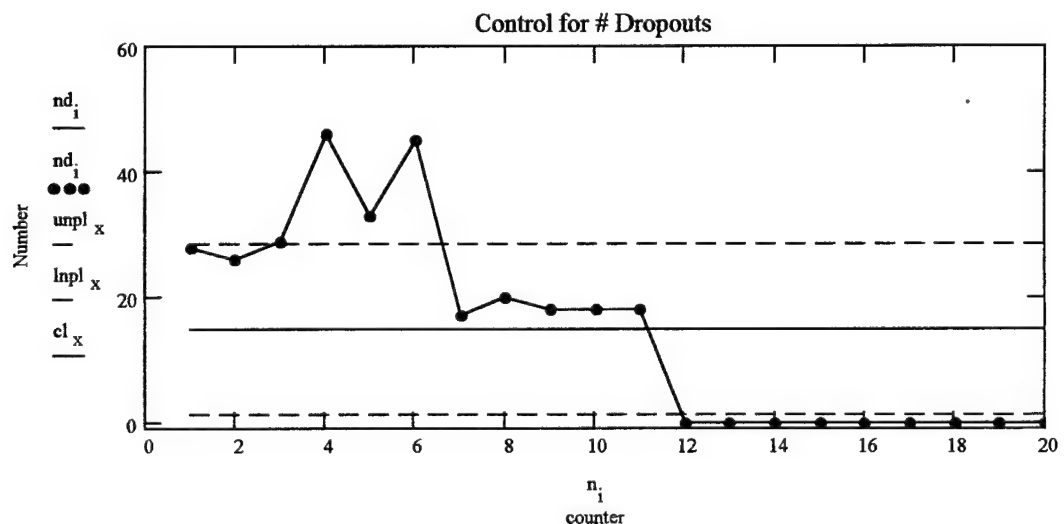


Figure 4.55 - Statistical control chart for number of dropouts over time for February 24, 1997

Figure 4.56, control chart for false returns, shows a set of false return values that are not centered about the mean and have runs both above and below the mean.

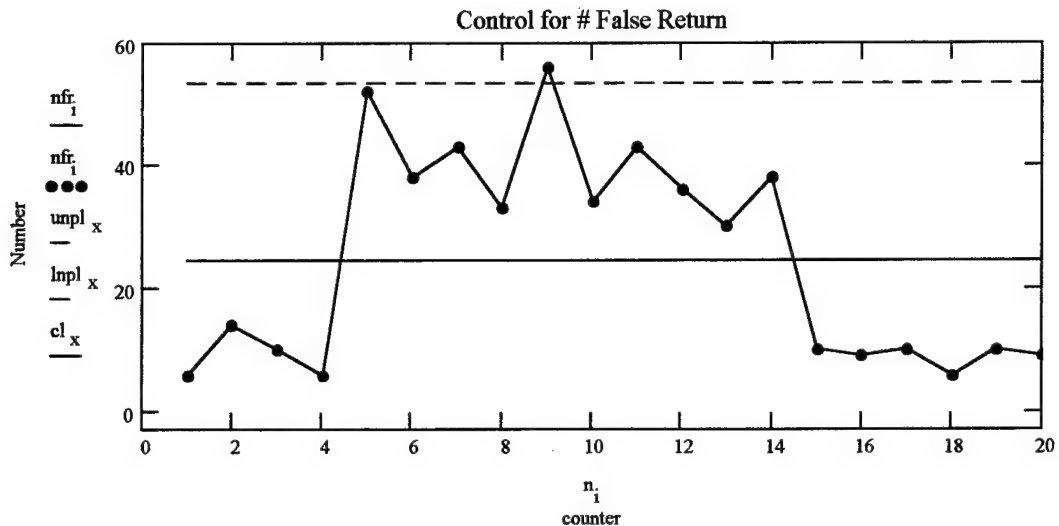


Figure 4.56 - Statistical control chart for number of false returns over time for February 24, 1997

Figure 4.57, control chart for rainfall rate, shows why the number of returns, both dropouts and false returns, is out of control. The rain is a factor in the erratic behavior of the system. Here we see that the rainfall rate is an erratic and unpredictable influence operating in the environment.

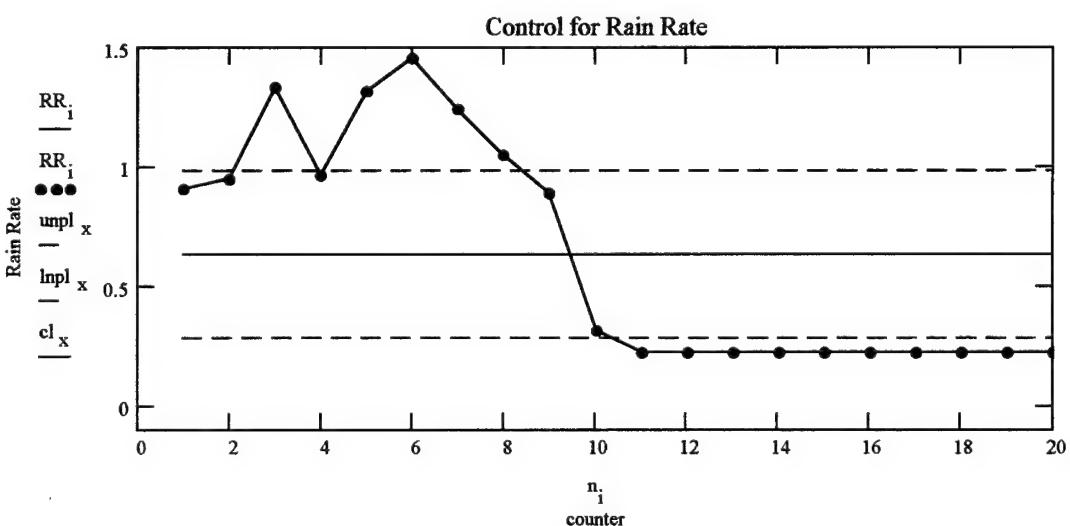


Figure 4.57 - Statistical control chart for rainfall rate over time on February 24, 1997

Like rainfall rate, visibility is also a very important influence on the performance on this day. Figure 4.58, control chart for visibility, shows that the process is not in control and that the behavior has a tendency to increase.

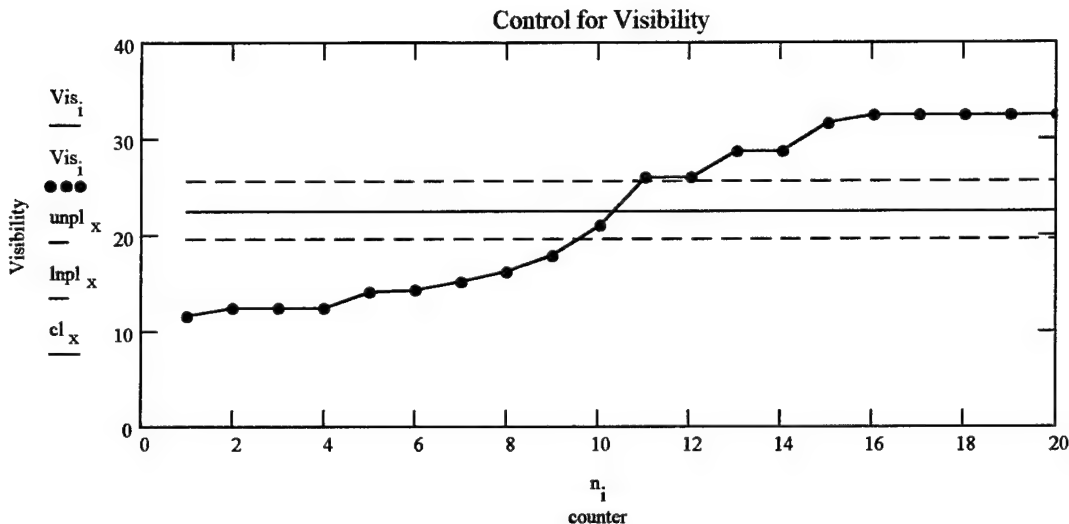


Figure 4.58 - Statistical control chart for visibility over time on February 24, 1997

4.3.4 - February 25, 1997

The control charts for number of dropouts, number of false returns, rain rate, and visibility for February 25th are pictured below, Figures 4.59-4.62. The data in Figure 4.59, control chart for dropouts, shows that the number of dropouts is not centered, with runs above and below the mean. Plus, there is a fairly wide 3-sigma limit.

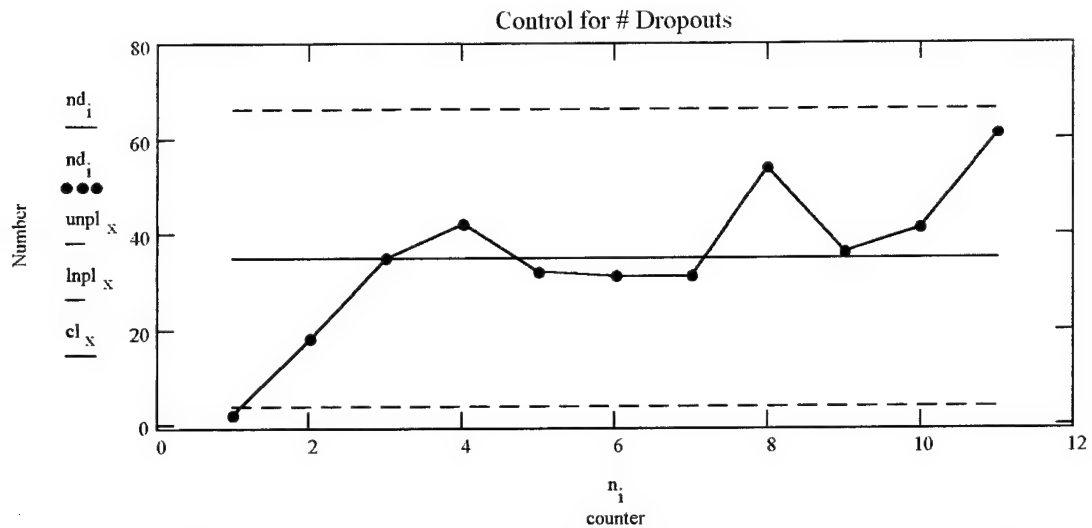


Figure 4.59 - Statistical control chart for number of dropouts over time for February 25, 1997

Figure 4.60, control chart for false returns, also has a wide 3-sigma limit, which makes it look like all the points fall within the limits. However, there are two large runs within the sample, one above and one below the mean, which demonstrates that the process, and the false returns, are being influenced.

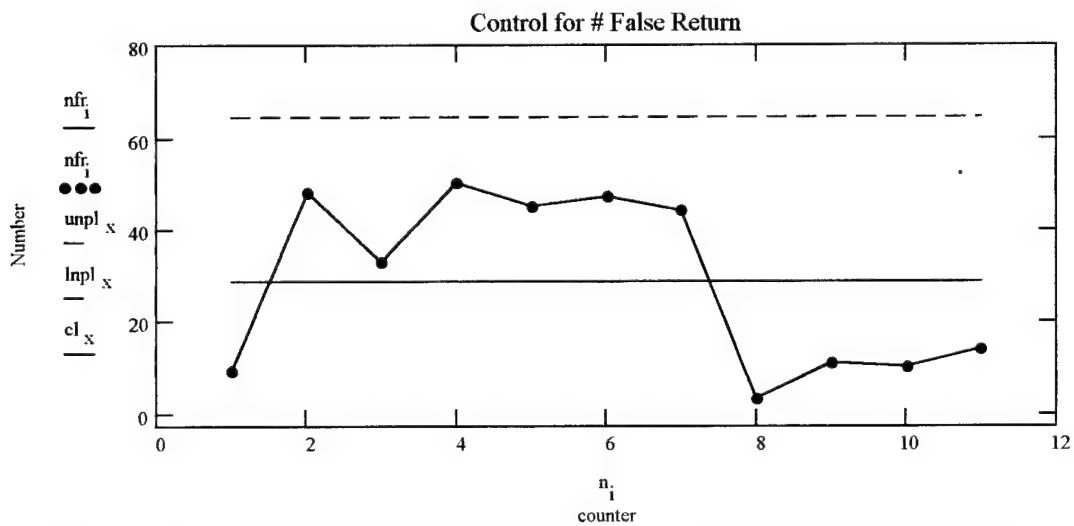


Figure 4.60 - Statistical control chart for number of false returns over time on February 25, 1997

All but one point falls within the 3-sigma limit in Figure 4.61, control chart for rainfall rate. But, the majority of the points are part of a long run located below the mean. This shows the rainfall rate decreasing.

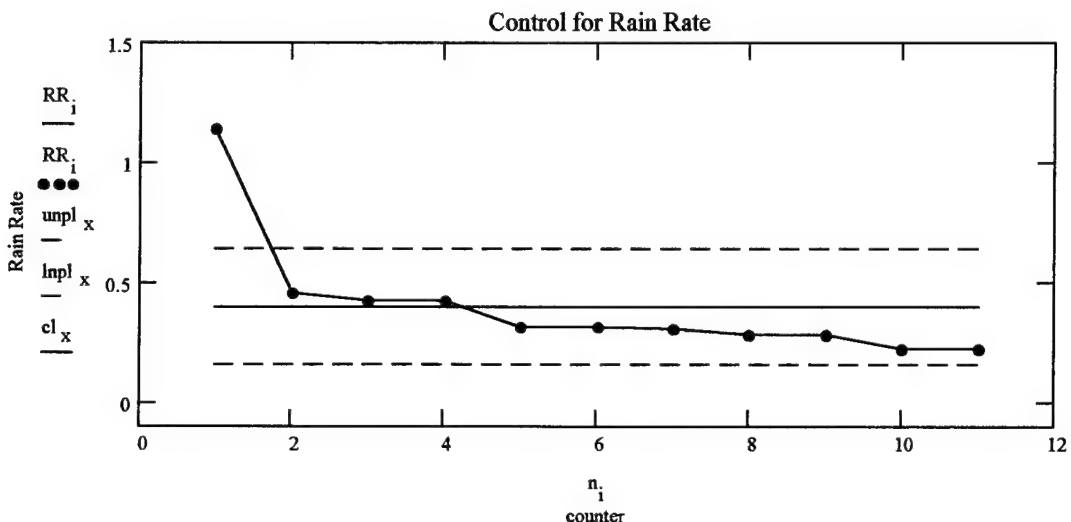


Figure 4.61 - Statistical control chart for rainfall rate over time on February 25, 1997

Finally, Figure 4.62, control chart for visibility, shows an initial run below the mean leading to a run above the mean. This shows the trend toward improved visibility over the period on the 25th.

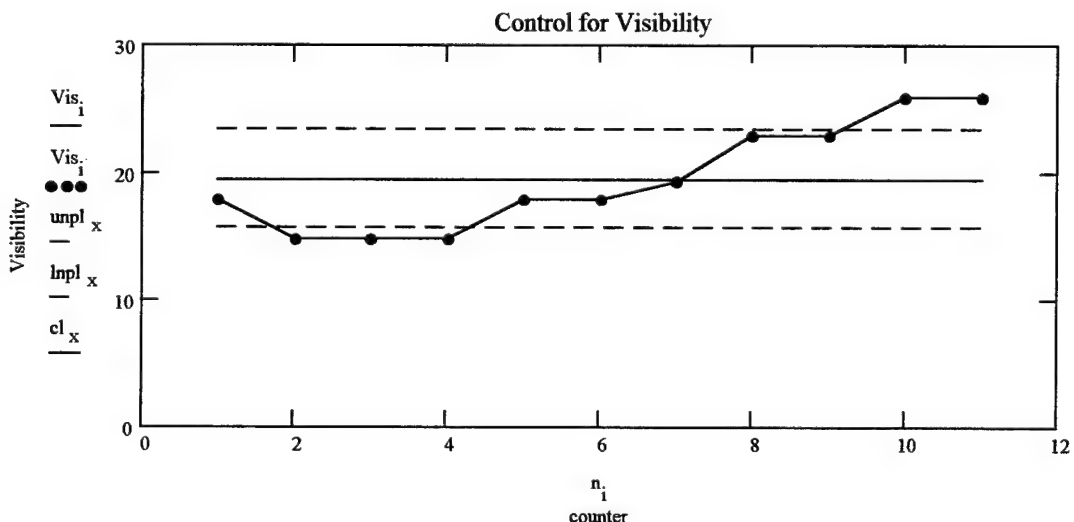


Figure 4.62 - Statistical control chart for visibility over time on February 25, 1997

4.3.5 - February 26, 1997

The control charts for number of dropouts, number of false returns, and visibility for February 26th are pictured below, Figures 4.63-4.65. In Figure 4.63, the control chart for dropouts shows a very wide 3-sigma limit, due to the high dropout counts early in the sample. Then, after the first few points, we see a quick trend to decrease.

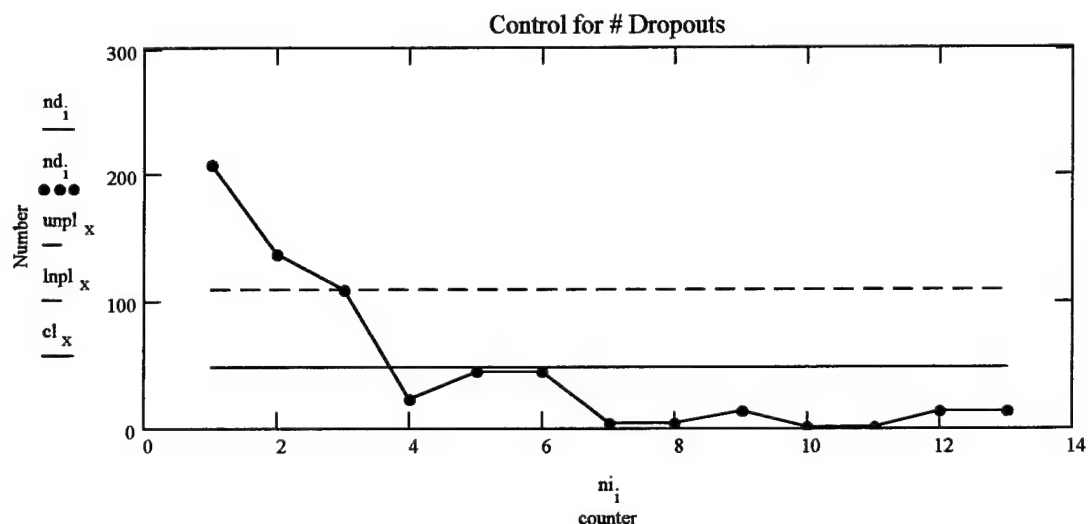


Figure 4.63 - Statistical control chart for number of dropouts over time on February 26, 1997

Figure 4.64, control chart for false returns, also has a wide 3-sigma limit, influenced by the range of values in the sample of false returns. There are also four runs, two above the mean and two below the mean.

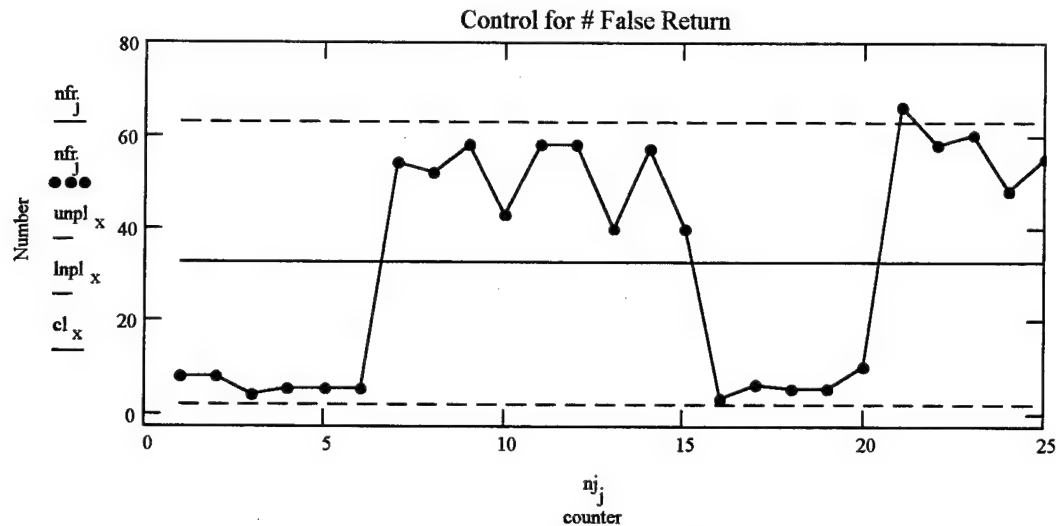


Figure 4.64 - Statistical control chart for number of false returns over time on February 26, 1997

Figure 4.65, control chart for visibility, shows that the visibility first runs below the mean then increases to run above the mean. This highlights the trend toward better visibility during the 26th.

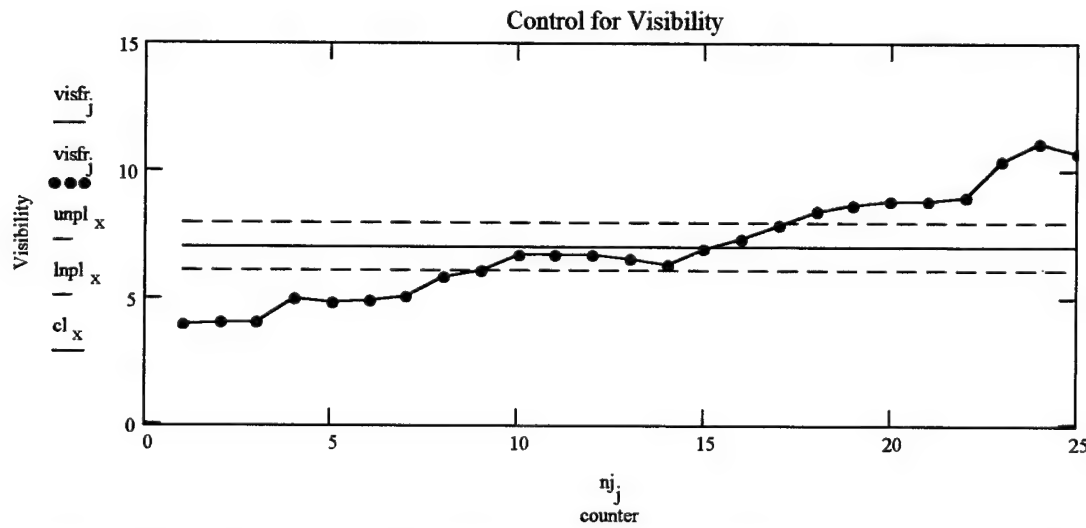


Figure 4.65 - Statistical control chart for visibility over time on February 26, 1997

4.3.6 - February 27, 1997

The control charts for number of dropouts, number of false returns, and visibility for February 27th are pictured below, Figures 4.66-4.68. In Figure 4.66, the control chart

for number of dropouts shows that the sample is dominated by a small group of points which fall well outside of the three sigma range.

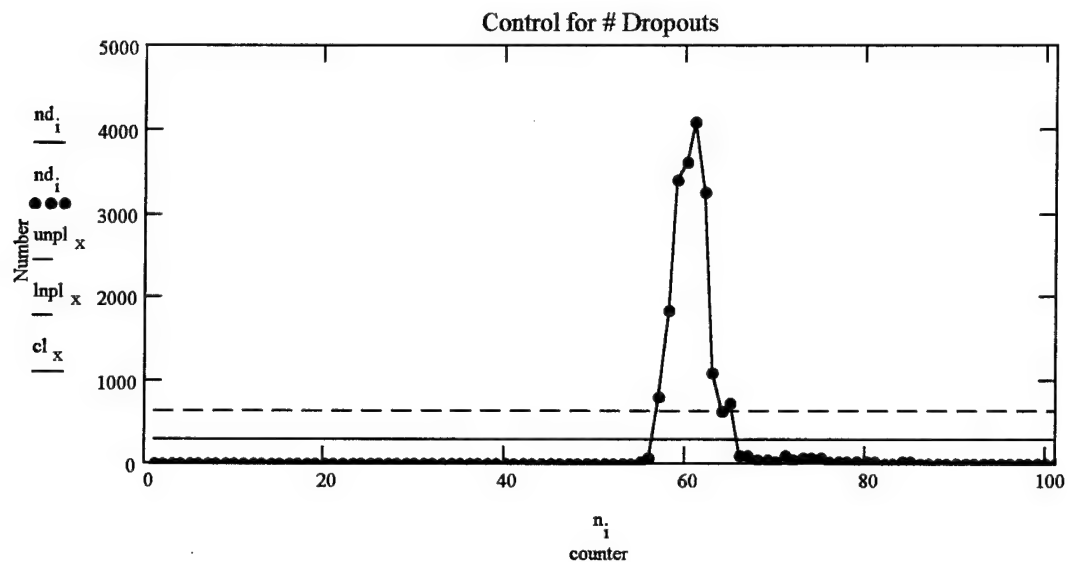


Figure 4.66 - Statistical control chart for number of dropouts over time for February 27, 1997

Figure 4.67 shows the control chart for the number of false returns. Like in the chart for dropouts, we see that a small group of points falls well outside of the three sigma limit. Plus, points at the beginning of the sample stay well below the mean.

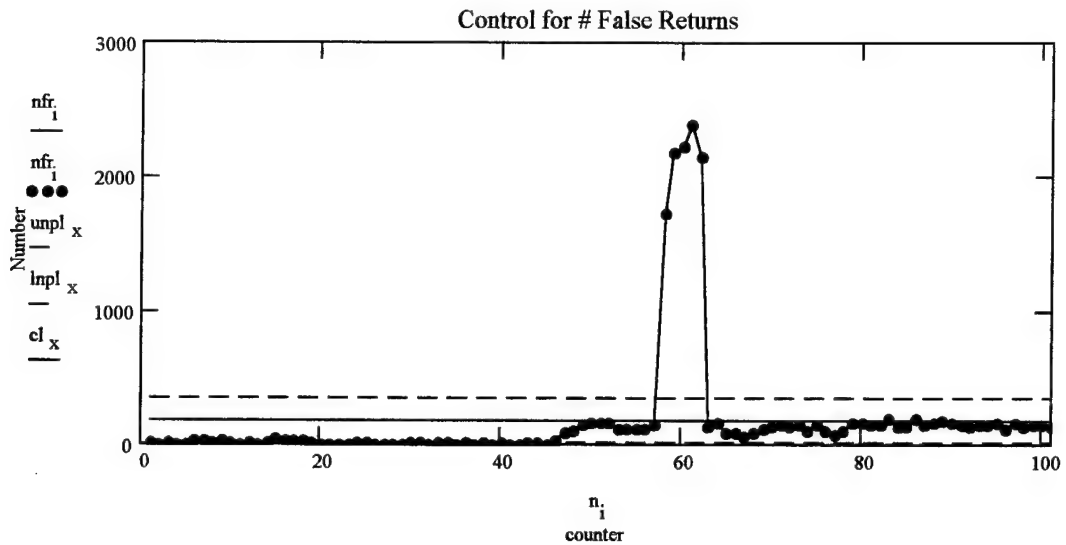


Figure 4.67 - Statistical control chart for number of false returns over time for February 27, 1997

Finally, Figure 4.68 shows the statistical control chart for the visibility. This chart highlights a trend toward lower visibility over time on this day. Initially, the visibility continues to decrease, then the values level out in the latter half of the sample.

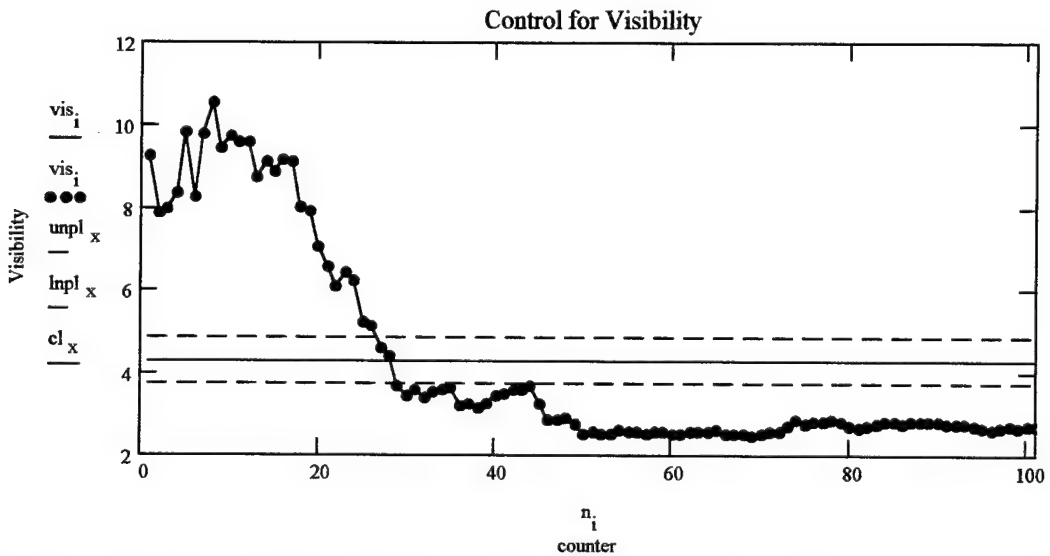


Figure 4.68 - Statistical control chart for visibility over time for February 27, 1997

4.3.7 - February 28, 1997

The control charts for number of dropouts, number of false returns, and visibility for February 28th are pictured below, Figures 4.69-4.71. In Figure 4.69, the control chart for dropouts shows that the majority of the dropouts fall below the mean while there are four points outside the 3-sigma limit.

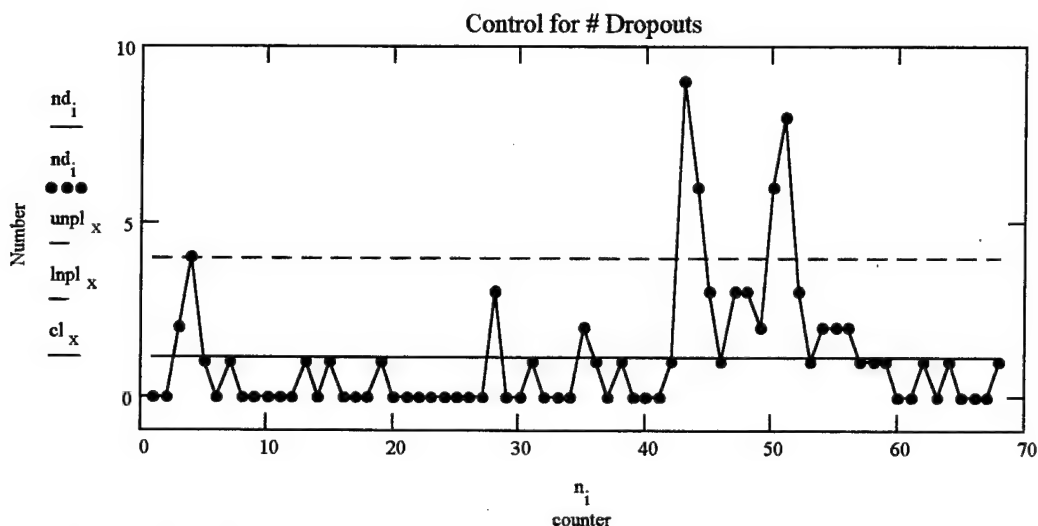


Figure 4.69 - Statistical control chart for number of dropouts over time on February 28, 1997

Figure 4.70, control chart for false returns, has a total of six runs in the false return data set. Three runs are below the mean, with two of them outside the 3-sigma limit; three runs fall above the mean, with two of them outside the 3-sigma limit.

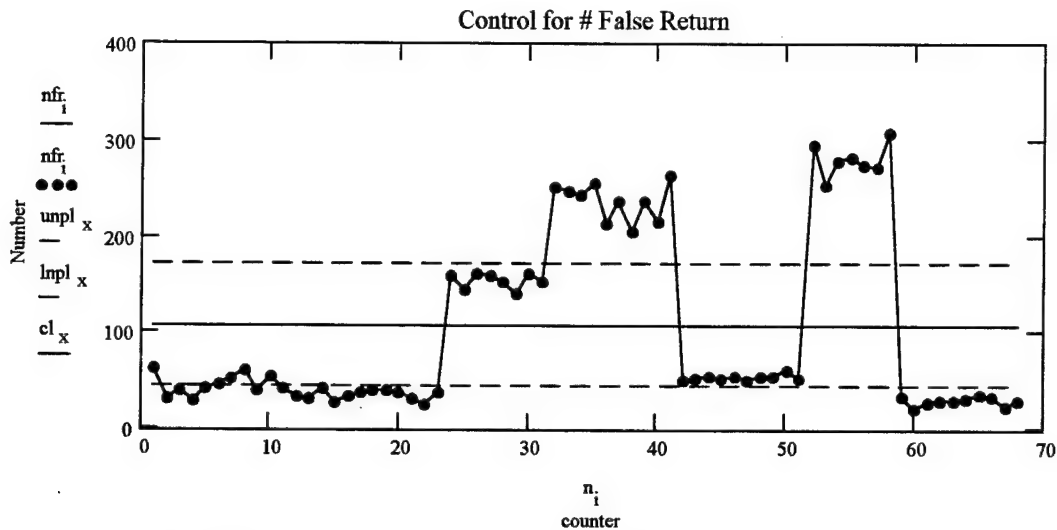


Figure 4.70 - Statistical control chart for number of false returns over time on February 28, 1997

Figure 4.71, control chart for visibility, identifies the increase in visibility seen over the day on the 28th. The data values start out well below the mean and end up well above the mean.

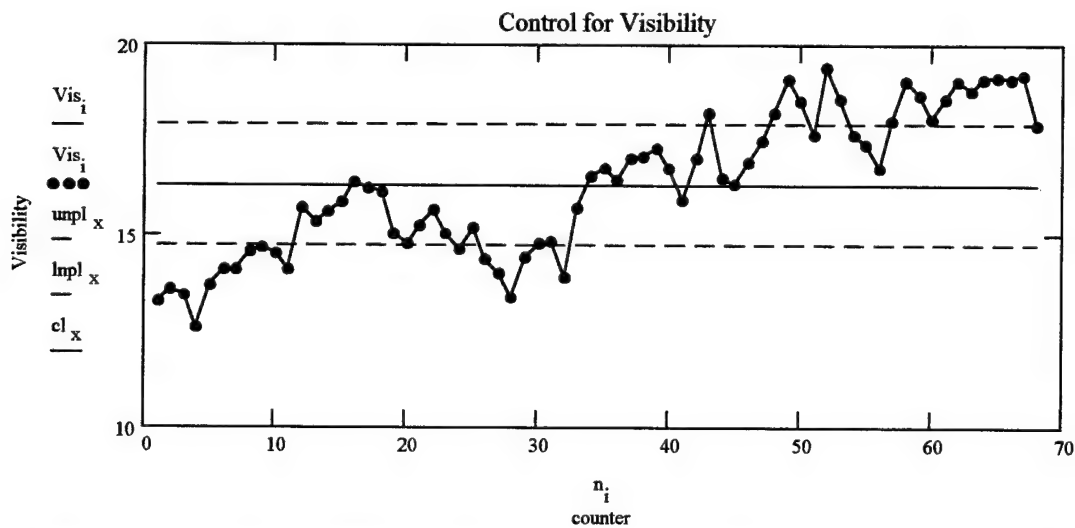


Figure 4.71 - Statistical control chart for visibility over time on February 28, 1997

4.4 - Mean Free Path and Survival Equation

The study of the mean free path and the survival equation allowed the understanding of the laser system to focus to a smaller scale. Particles in the atmosphere

cause degradation of the ladar image, but no size distribution data was collected on the characteristics of these particles. So by assuming a Marshall-Palmer raindrop distribution, we were able to more specifically analyze the behavior of the laser beam in the atmosphere. Since mean free path describes how far the beam will travel, on average, before it first hits a raindrop, this shows how much atmospheric penetration occurs before we get a false return. The survival equation then tells us, over the entire path of the laser, how many returns we should expect to see in the image, assuming that the beam energy is scattered back to the laser. Both of these concepts together help to solidify the ideas on the performance of the system during weather events.

4.4.1 - Mean Free Path for Each Day

Using the derived mean free path equation given in Section 3.4.4, values for mean free path were calculated for February 24th and 25th, the two rainfall days. A Marshall-Palmer distribution of raindrops, shown in Figure 4.72, was used in order to compute the mean free path, since raindrop size data was unavailable.

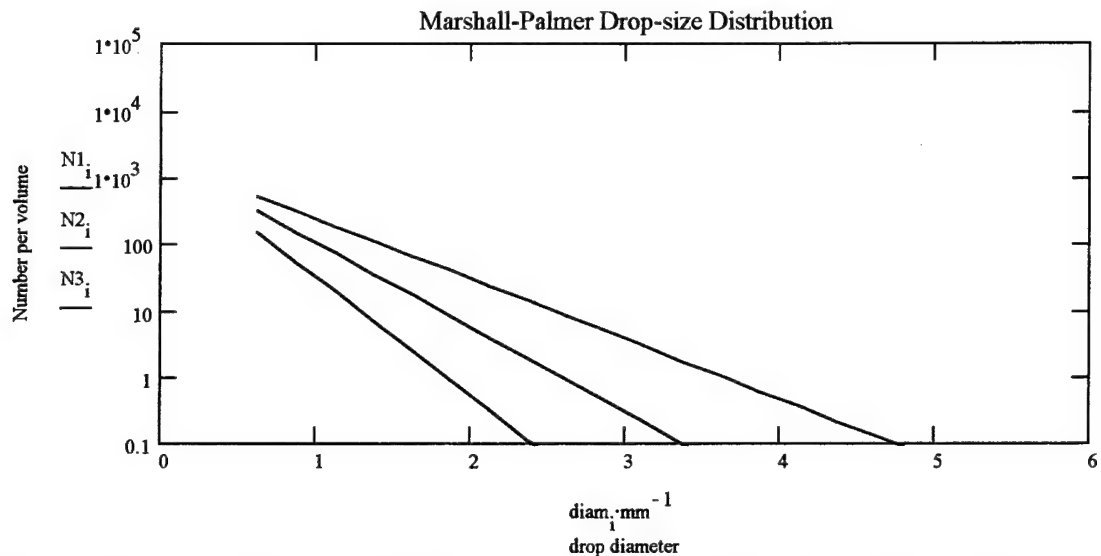


Figure 4.72 - Marshall Palmer raindrop size distribution, taking into three rainfall rates:
1 mm/hr, 5 mm/hr, and 5 mm/hr from left to right

An array of rainfall rates for a particular day was used in the mean free path equation to produce an array of mean free paths. This mean free path array displayed how the mean free path and rainfall rate were simultaneously changing with time. Table 4.6 includes the mean free path arrays computed for the 24th and 25th. We can see that the value of the mean free path varied since the rain rate changed over time. Maximum values are found at the end of the data set, where the rain has pretty much ended.

24-Feb	25-Feb
2.283	1.862
2.161	4.008
1.640	4.281
2.124	4.281
1.662	5.527
1.534	5.527
1.739	5.640
1.994	6.071
2.273	6.071
5.575	7.588
7.620	7.588

Table 4.6 - Mean free path, in kilometers, on February 24, 1997 and February 25, 1997 as it changes over time. This calculation assumes that the laser beam hits a drop of any size, causing a false return to be registered by the system.

4.4.2 - Survival Equation and Calculated Number of Returns

Once the mean free path array was generated, the survival equation was used to compute the number of false returns expected for each mean free path. The calculated number of false returns would then be compared to the actual number of false returns in the ladar images. This comparison would then either verify or refute assumptions about the sizes of the raindrops causing the false returns seen in the images. Table 4.7 shows the number of returns computed using the survival equation for February 24th and 25th. The number of returns changes since the rain rate was not constant during the time period. In fact, the number of returns is a minimum at the end of the data set since the minimum rainfall rates were at this time as well.

24-Feb	25-Feb
572	657
587	352
719	333
595	333
713	264
753	264
690	260
624	243
565	243
262	197
197	197

Table 4.7 - Number of false returns computed using the survival equation for February 24, 1997 and February 25, 1997

4.4.3 - Minimum Diameter Calculations

When the results from Section 4.4.2 were compared to the actual data, it was found that the computed number of false returns was over an order of magnitude greater than the actual number of false returns recorded. So, we set out to determine the minimum diameter of the drops causing the false returns. In the previous calculations, all size drops were included in the raindrop size distribution. Now, certain drops below this minimum diameter would be disregarded. We would know we found the correct minimum diameter when the number of false returns calculated was of the same order of magnitude as the number of false returns seen in the images. Regression was used to find this diameter, and a value of 3.0 mm worked well for both rainfall days. To speed up mean free path calculations, all but one of the 0.224 mm/hr rainfall rates at the end of the rainfall rate data set were deleted. Once the mean free path array was calculated using the raindrops larger than the 3.0-mm minimum diameter, it was inserted into the survival equation to compute an array including the number of false returns.

Table 4.8 shows the revised mean free path arrays for February 24th and 25th. The mean free path, once again, fluctuates as the rainfall rate changes. However, as we reach the last mean free path, the value decreases. This value is computed with the lightest rainfall rate, so it should be the longest mean free path. This reflects the use of the minimum diameter of concern.

24-Feb	25-Feb
218.183	118.105
193.823	1338.997
78.065	1448.765
183.089	1448.765
81.454	1271.601
62.992	1271.601
94.386	1228.001
148.108	1057.656
229.878	1057.656
1253.308	571.503
563.939	571.503

Table 4.8 - Mean free path, in kilometers, computed with the 3.0-mm minimum diameter for February 24, 1997 and February 25, 1997. This calculation assumes that the laser beam hits a drop larger than 3.0 mm and causes a false return.

Table 4.9 shows the revised number of false returns calculated from the survival equation for February 24th and 25th. By using a modified raindrop size distribution, the number of false returns calculated was within the same order of magnitude as the number of false returns seen in the ladar images. We see a similar pattern in number of false returns as we saw in mean free path. The number changes with the mean free path and the rainfall rate, and we also see the slight increase in the number of false returns in the last value.

24-Feb Survival	24-Feb Data	25-Feb Survival	25-Feb Data
7	6	13	9
8	14	1	48
20	10	1	33
9	6	1	50
20	52	1	45
25	38	1	47
17	43	1	44
11	33	2	3
7	56	2	11
1	34	3	10
3	43	3	14

Table 4.9 - Number of false returns computed with the 3.0-mm minimum diameter and actual data values for false returns for February 24, 1997 and February 25, 1997

4.4.4 - Use of Theoretical Rainfall Rate Distribution

Once the mean free path and survival equation analysis was done on the data available, a theoretical rainfall rate distribution was used. This distribution covered a wider spread of rainfall rates, thus allowing an opportunity to see the behavior of the system in several weather scenarios. The 3.0-mm minimum diameter was used when computing the mean free path array with this rainfall rate array. Table 4.10 contains the rainfall rate in mm/hr, mean free path in km, and calculated number of false returns for the theoretical distribution.

Rain Rate	Mean Free Path	Number
1	167.616	10
2	28.986	54
3	11.522	133
4	6.247	236
5	3.974	355
8	1.63	722
10	1.097	925
12	0.803	1069
15	0.556	1171
18	0.417	1157
20	0.354	1101
23	0.287	977
25	0.254	879
27	0.227	778
30	0.195	632
32	0.178	541
35	0.157	422
38	0.14	322
40	0.131	266
42	0.122	219
45	0.111	161

Table 4.10 - Theoretical rainfall rate distribution(mm/hr), mean free path (km), and calculated number of false returns

Mean free path reflects the increase in the rainfall intensity by decreasing; however, the number of returns hits a peak near 15 mm/hr. Even when the distance interval is decreased, this peak still appears. This is due to the fact that the minimum distance is set at 500 m. After the 15 mm/hr rainfall rate, the mean free path ceases to reach this minimum threshold. The laser beam never reaches the target, so the number of false returns decreases. The mean free path behaves as expected—as the rainfall rate increases, the mean free path continues to decrease.

4.5 - Solar Contamination in the Operation of the Ladar System

Once the 3.0-mm minimum diameter was determined, a calculation was performed to reconfirm that this diameter caused the false returns seen. So taking into account that the beam diameter was 2.0 cm, the drop diameter was 3.0 mm or larger, and the receiver diameter was 4 inches, a series of calculations could determine the power return from these 3.0-mm drops. In order to do this, we need to focus on the portion of the drop which scatters radiation directly back to the detector. This excludes any energy not scattered directly back to the detector, scattered energy not seen by the detector. First, the angle which includes this scattered energy was calculated

$$\alpha = \frac{\frac{diam_{reciever}}{2}}{range} = 1.17 * 10^{-4}$$

where the range was set to 400m. With this number, the solid angle of this portion of the drop can then be calculated.

$$\Omega_{spot} = 2 \pi \left(1 - \cos\left(\frac{\alpha}{2}\right) \right) = 1.267 * 10^{-8} \text{ sr}$$

Next, the area of the spot on the drop needed to be determined.

$$area = \Omega_{spot} \left(\frac{\frac{diam_{drop}}{2}}{2} \right)^2 = 2.85 * 10^{-8} \text{ mm}^2$$

Now, the power reflected by this spot on the drop was calculated. First, the percentage reflected by the drop was determined by considering multiple scattering. As the laser beam intercepted the drop, a portion would be scattered by the front face of the drop. The remainder would travel into the drop where a portion of that energy would be scattered back toward the front of the drop by the back face of the drop. Finally, as this

energy traveled back through the front face of the drop a portion of this energy would be scattered back. At this point, a simple formula was constructed to account for all scattering taking place inside and outside of the drop, assuming that a water interface scatters 5% of the energy ($r = 0.05$).

$$\text{power reflected} = \%refl = r + (r + r^3 + r^5) * (1 - r)^2 = 9.524 \%$$

Now that this value had been determined, the power scattered back to the receiver by the spot on the 3.0-mm drop was calculated. The area of the spot, the power in the beam, and the power reflected are multiplied together to determine this value.

$$\text{power in the beam} = \text{power} = \frac{2000 \text{ W}}{\pi \left(\frac{\text{diam}_{beam}}{2} \right)^2} = 6.366 * 10^6 \text{ W m}^{-2}$$

$$\text{scattered energy} = \text{area} * \text{power} * \%refl = 17.281 \text{ nW}$$

Surprisingly, this 17.281 nW return was below the approximate 72 nW which was the minimum return detectable by the system. In fact, when these calculations were worked backwards, starting with a 72 nW return, a drop with a diameter of 6.12 mm was causing the minimum return. Since a 6.12-mm drop was much larger than the drops we determined were causing the returns, the source of this discrepancy needed to be determined.

The ladar system sent out a beam at a 1.06- μm wavelength; however, the detector was sensitive to any return wavelengths between 0.4 μm and 1.1 μm . Unfortunately, this is also a wavelength band in which the sun is a very strong emitter. So, it needed to be determined whether radiation from the sun, scattered by particles in the atmosphere, was contaminating the images.

First, two values needed to be determined for the wavelength band of concern, 0.4 μm to 1.1 μm . Plank's function, L_{sun} , and extinction, β , showed the amount of radiance present in the wavelength band.

$$L_{\text{sun}_i} = \frac{2 * h * c^2}{\lambda_i^5 * \left(\exp\left(\frac{h * c}{k * \lambda_i * T_S}\right) - 1 \right)}$$

$$\beta_i = 10^{-3} * (\lambda_i)^{-4}$$

where

$$h = 6.629 * 10^{-34} \text{ J sec}$$

$$c = 2.99 * 10^8 \text{ m sec}^{-1}$$

$$T_S = 5770 \text{ K}$$

Extinction was used to calculate the radiance of the airlight for a black distant object at a distance $s = 200 \text{ km}$. But first, the solid angle of the sun needed to be determined.

$$\Omega_{\text{sun}} = \frac{\pi * r_{\text{sun}}^2}{dist_{\text{sun}}^2} = 6.842 * 10^{-5} \text{ sr}$$

where

$$r_{\text{sun}} = 7 * 10^5 \text{ km}$$

$$dist_{\text{sun}} = 150 * 10^6 \text{ km}$$

Therefore,

$$L_{\text{air}_i} = L_{\text{sun}_i} * \frac{\Omega_{\text{sun}}}{4 * \pi} * \left(1 - \exp(\beta_i * s) \right)$$

Figure 4.73 below shows the radiance of the sun, L_{sun} , and the air, L_{air} , over the wavelength band in question.

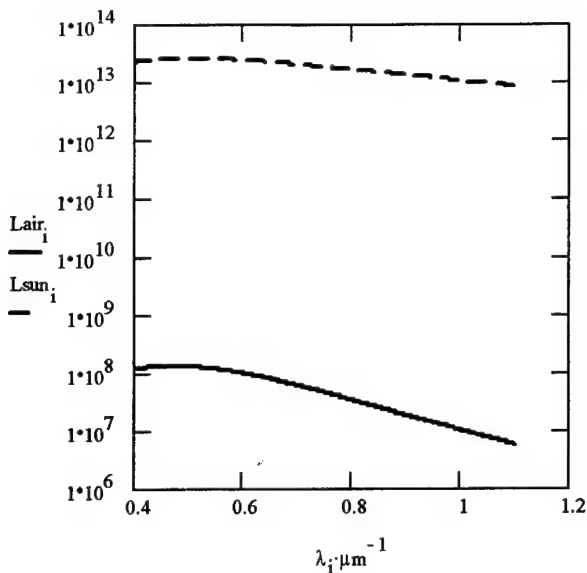


Figure 4.73 - Comparison of the radiance of the sun (dashed line) to the radiance of a black object (solid line) at 200 km (at the horizon). We can see that the airlight is several orders of magnitude less than the light from the sun in this wavelength band. This makes sense since the horizon is not nearly as bright at the sun.

Next, three values needed to be determined to find out how much solar radiation was being scattered back toward the detector. First, the radiance from the sun within the wavelength band was calculated. A $d\lambda$ of 10^{-3} μm helped us to remain within our wavelength band.

$$Radsun = \sum_{i=400}^{1100} L_{sun_i} * d\lambda = 1.289 * 10^7 \text{ W m}^{-2}$$

Second, the airlight within the wavelength band was determined.

$$Airlight = \sum_{i=400}^{1100} L_{air_i} * d\lambda = 43.951 \text{ W m}^{-2}$$

Finally, the radiance of the sun over the full wavelength spectrum was defined using the Stefan-Boltzmann equation

$$Fullsun = \frac{\sigma * T_s^4}{\pi} = 2.001 * 10^7 \text{ W m}^{-2}$$

where σ is the Stefan-Boltzmann constant, $5.67 * 10^{-8} \text{ W m}^{-2} \text{ K}^{-4}$.

From these three values, three other values were resolved. First was the total energy reaching the earth, which was related to the solid angle of the sun.

$$Fullsun * \Omega_{sun} = 1.369 * 10^3 \text{ W m}^{-2}$$

This value is also referred to as the solar constant. Second, the total energy reaching the earth in our particular wavelength band was found, also depending on the solid angle of the sun.

$$Radsun * \Omega_{sun} = 822.177 \text{ W m}^{-2}$$

Finally, the airlight in the wavelength band was calculated; however, upon further examination, it was determined that this value was the same as the value determined earlier for *Airlight*, 43.951 W m^{-2} . This is the radiance at the horizon.

To do the next set of calculations, some further information about the laser beam needed to be answered. We knew that the beam had a divergence, so the diameter of the beam, or the beam waist, at a certain distance from the source was determined. The first step was to assume a situation where there was a 0.5-km high ceiling and a 10-m tree 1 km from the laser. Through some elementary geometry, it was found that the laser intersected the ceiling 50 km downrange. Next, the value of z_0 was calculated

$$z_0 = \frac{\pi * \omega_0^2 * n}{\lambda} = \frac{\pi * (2\text{cm})^2 * 1.000334}{1.06\mu\text{m}} = 1.186 * 10^3 \text{ m}$$

where ω_0 is the original beam diameter, n is the index of refraction, and λ is the laser wavelength. Now that z_0 was determined, the beam waist, ω , at $z = 50$ km could be determined through the following formula.

$$\omega = \sqrt{\omega_0^2 * \left(1 + \frac{z^2}{z_0^2}\right)} = 0.843 \text{ m} = 84.3 \text{ cm}$$

Once the beam waist was found, the specific levels of radiation reaching the detector from our patch of clouds was calculated. First, the solid angle of the detector was determined

$$\Omega_{\text{det}} = \frac{\pi * \omega^2 * 1.2}{4 * z^2} = 2.682 * 10^{-10} \text{ sr}$$

where 1.2 was inserted since the field of view of the detector was 20% greater than the beam waist. Next, the radiation from the air reaching the detector was ascertained.

$$Airlight * \Omega_{\text{det}} = 11.788 \text{ nW m}^{-2}$$

And the clouddlight was specified, assuming that on a cloudy day the irradiance on a pyranometer would be approximately 300 W m^{-2} .

$$Cloudlight = \frac{300 \text{ W m}^{-2} * \Omega_{\text{det}}}{2 * \pi} = 12.806 \text{ nW m}^{-2}$$

These two values, *Airlight* and *Cloudlight*, are of the same order of magnitude, plus, we see that a cloudy sky scatters more energy toward the detector than clear air. So a day with a weather event is more likely to introduce sun contamination into the images. Plus, when this value is added to the energy scattered by the spot on the raindrop (17.281 nW)

calculated earlier we see that our scattered energy is still less than the 72 nW needed to trigger a false return.

A final calculation was done to see how many drops were within the laser cone to scatter the solar energy. The volume of air the laser cone sees was

$$Volume = \frac{\pi}{3} * \left(\frac{\omega}{2}\right)^2 * z = 9.313 * 10^3 \text{ m}^3$$

Next, using three different rainfall rates, a number density distribution for a drop diameter distribution was determined using the survival equation. Tables 4.11-4.13 show the drop sizes and number densities for a 1, 5, and 10-mm/hr rainfall rate.

Table 4.11

Drops (mm)	Number density (#/m ³)
0.5	1.03E+03
1.5	17.068
2.5	0.283
3.5	4.69E-03
4.5	7.77E-05
5.5	1.29E-06

Table 4.12

Drops (mm)	Number density (#/m ³)
0.5	1.85E+03
1.5	99.581
2.5	5.348
3.5	0.287
4.5	0.015
5.5	8.29E-04

Table 4.13

Drops (mm)	Number density (#/m ³)
0.5	2.26E+03
1.5	180.393
2.5	14.398
3.5	1.149
4.5	0.092
5.5	7.32E-03

Tables 4.11 through 4.13 - Drop distribution and number density for 1-mm/hr, 5-mm/hr, and 10-mm/hr rainfall rates, respectively.

Then, the total cross sectional area of the drops within the cone was calculated for each of the three rainfall rate cases. The formula was

$$\sigma = \left[\sum_{i=0}^5 N_i * \pi * (diameter_i)^2 \right] * Volume$$

Table 4.14 shows the three cross sectional areas computed.

Rainfall rate (mm/hr)	σ m^2
1	8.71
5	21.207
10	31.512

Table 4.14 - Total cross sectional area, in m^2 , of the raindrops within the laser beam cone for the three rainfall rates. As the rainfall rate increases, so does the total cross sectional area, since more drops are present.

Finally, the expected number of drops within the laser beam cone was determined, since we knew the area of the beam and the cross sectional area of the drops within that cone.

The equation was

$$number = \frac{\sigma}{\pi * \left(\frac{\omega}{2}\right)^2}$$

Table 4.15 displays the number of drops between the laser and the portion of sky 50 km away from it, according to rainfall rate.

Rainfall rate (mm/hr)	Number of drops
1	16
5	38
10	56

Table 4.15 - Number of drops calculated to be within the laser beam, according to rainfall rate. As is expected, when the rainfall rate increases, there are more drops within the beam.

So, it was shown that there were drops present within the laser beam capable of scattering the laser energy as well as solar energy. The scattering particle could be a

raindrop on the test range scattering laser energy or a raindrop well off in the distance scattering solar energy. The system fails to recognize where that false return is located since it is unable to distinguish between energy scattered back from the laser beam and energy scattered from the sun.

V. Summary, Conclusions, and Recommendations

5.1 - Summary

This thesis involved a study of the performance of laser imaging radar in rain and fog. The weather is an important factor in determining how clear an image the ladar will produce, so information providing insight into the specific effects of the atmosphere helps in fine tuning the system. It was seen that raindrops and fog droplets do disrupt the clarity of the images, but not to a serious degree when assuming small rainfall rates. Also, an analysis of mean free path led to an understanding of the size of droplets potentially causing returns and the number of returns caused by rainfall events. Finally, by a more careful study of the energy picked up by the ladar detector, it was found that solar energy was contaminating the images produced by the ladar.

5.2 - Conclusions

While studying the image disruption, false returns and dropouts were the focus of the work. Even though the weather events in question were not very severe, disruption of the images still appeared. This disruption needs to be minimized to allow the ladar system to operate successfully.

The mean free path analysis provided more insight into the propagation of the laser beam into the atmosphere. The mean free path showed a good response to changes in the rainfall rate, as would be expected, plus a study of the survival equation described the effects of the raindrops more specifically. The information derived from the mean free path and the survival equation led to an investigation of a minimum drop diameter of

concern. By determining a minimum diameter for drops causing returns, a better picture of the raindrop size distribution could be drawn.

Also, the discovery of the minimum sized drop led to the hypothesis of solar radiation contamination into the ladar system. This contamination was possibly a consequence of the setup of the system, and due to the possible introduction of solar radiation, it was found that the system failed to distinguish between scattered solar and laser energy. However, the absence of solar radiation data limited the work on this issue to generalized calculations.

5.3 - Recommendations

From this thesis work, two recommendations emerged. One, a fuller study into the weather effects needs to be accomplished. A new study needs to take more days into account, maybe even a full year of data, as well as days with no significant weather. This would provide a better picture of the performance of the system, since it would include more data over a greater variety of days. Since the final goal of the study is to quantify the effect of weather on the ladar, the use of a larger data set would make the development of a prediction equation for the performance of the system easier. Plus, the inclusion of fog and raindrop size distributions in the weather data sets would make the analysis of mean free path and the survival equation more accurate. And two, the solar contamination issue needs better definition. The recording of actual solar radiation would help define the problem better and make the calculations more accurate. Plus, if this issue was more accurately explored, it could be determined if the solar contamination is indeed a serious problem able to be corrected.

References

Chylek, Petr, 1977: Extinction and Liquid Water Content of Fogs and Clouds. *Journal of the Atmospheric Sciences*, **35**, 296-300.

Devore, Jay L., 1995: *Probability and Statistics for Engineering and the Sciences*. Duxbury Press, 743 pp.

Huschke, Ralph E., 1959: *Glossary of Meteorology*. American Meteorological Society, 638 pp.

Jelalian, Albert V., 1992: *Laser Radar Systems*. Artech House, 292 pp.

Keller, John, March 15, 1993: Will Ladar be the DoD's Next Quantum Leap?. *Military & Aerospace Electronics*, 25-27.

Kyle, Thomas G., 1991: *Atmospheric Transmission, Emission, and Scattering*. Pergamon Press, 287 pp.

Pinnick, R.G., 1978: Vertical Structure in Atmospheric Fog and Haze and Its Effects on Visible and Infrared Extinction. *Journal of the Atmospheric Sciences*, **35**, 2020-2032.

Pinnick, R.G., S.G. Jennings, Petr Chylek, H.J. Auvermann, 1979: Verification of a Linear Relation between IR Extinction, Absorption and Liquid Water Content of Fogs. *Journal of the Atmospheric Sciences*, **36**, 1577-1586.

Sears, Francis W. and Gerhard L. Salinger, 1975: *Thermodynamics, Kinetic Theory, and Statistical Thermodynamics*. Addison-Wesley Publishing Company, 454 pp.

Tonna, Glauco, 1991: Backscattering, Extinction and Liquid Water Content in Fog: A Detailed Study of Their Relations for Use in Lidar Systems. *Applied Optics*, **30**, 1132-1140.

Wheeler, Donald J. and David S. Chambers, 1992: *Understanding Statistical Process Control*. SPC Press, 406 pp.

Vita

Lt. Kathleen M. Campbell was born at Travis AFB, California on February 5, 1974. She grew up all over the country and the world as the daughter of an Air Force pilot. She has lived in California, Alabama, Illinois, Virginia, and Germany. She graduated from Ramstein American High School, Ramstein, Germany in 1992, and then went on to The Pennsylvania State University with an Air Force ROTC scholarship. While there, she was a member of the Penn State Marching Blue Band, Irvin Hall, and the Campus Weather Service. As an Air Force ROTC cadet, she was active in Arnold Air Society and served as Cadet Wing Commander. She graduated with a Bachelor of Science degree in Meteorology and Air Force Commission in 1996. Her first assignment was to the School of Engineering, Air Force Institute of Technology, Wright-Patterson Air Force Base, Ohio as a masters degree student in meteorology.

Lt. Campbell is married to Lt. Andrew Campbell of Wyoming, PA. Her parents, Col. (Ret.) James M. and Patricia A. Murphy live in O'Fallon, IL.

1. AGENCY USE ONLY (Leave blank)	2. REPORT DATE	3. REPORT TYPE AND DATES COVERED	
	March 1998		
4. TITLE AND SUBTITLE Performance of Imaging Laser Radar in Rain and Fog			5. FUNDING NUMBERS
6. AUTHOR(S) Kathleen M. Campbell, 2Lt, USAF			
7. PERFORMING ORGANIZATION NAME(S) AND ADDRESS(ES) AFIT/ENP 2950 P Street Wright-Patterson AFB, OH 45433 DSN 785-3636 x4682 Attn: Mai Cliff Dungev, cdungev@afit.af.mil			8. PERFORMING ORGANIZATION REPORT NUMBER AFIT/GM/ENP/98M-07
9. SPONSORING/MONITORING AGENCY NAME(S) AND ADDRESS(ES) WLMNGS 101 W. Eglin Blvd Suite 219 Eglin AFB, FL 32542-6810 DSN 872-1726 Attn: Mai Jeff Grantham, grantham@eglin.af.mil			10. SPONSORING/MONITORING AGENCY REPORT NUMBER
11. SUPPLEMENTARY NOTES			
12a. DISTRIBUTION AVAILABILITY STATEMENT Distribution Unlimited		12b. DISTRIBUTION CODE	
13. ABSTRACT (Maximum 200 words) The Air Force is currently developing imaging laser radar systems (ladar) for use on precision guided munitions. Scientists at Eglin Air Force Base are testing a 1.06 micrometer wavelength ladar system and need to understand the weather effects on the images. As the laser beam propagates through the atmosphere, fog droplets and raindrops cause image degradations - dropouts or false returns. Analysis of the dropouts and false returns helped to quantify the performance of the system in adverse weather conditions. Statistical analysis of the images showed non-linear relationships between variables, plus graphical analysis demonstrated the behavior of the dropouts and false returns with changing weather conditions. A study of mean free path and the survival equation was done by focusing on the false return data. This led to the hypothesis that raindrops with a diameter of 3.0 mm and larger were causing the false returns in the images. Further analysis revealed a 3.0-mm drop was not capable of scattering enough energy to be detected by the system. It was then hypothesized that the detector was also picking up solar energy scattered by raindrops, and the detector was unable to distinguish between solar and laser energy scattered by raindrops.			
14. SUBJECT TERMS Imaging Laser Radar, Wright Laboratory		15. NUMBER OF PAGES 112	16. PRICE CODE
17. SECURITY CLASSIFICATION OF REPORT Unclassified	18. SECURITY CLASSIFICATION OF THIS PAGE Unclassified	19. SECURITY CLASSIFICATION OF ABSTRACT Unclassified	20. LIMITATION OF ABSTRACT UL